

**Ocean mesoscale eddy phase speeds in a two-layer quasigeostrophic model  
and observations**

Lei Wang\* and Malte Jansen

*University of Chicago, Chicago, Illinois*

Ryan Abernathey

*Columbia University, New York, NY*

\*Corresponding author address: Lei Wang, Department of the Geophysical Sciences, University of Chicago, 5734 S. Ellis Avenue, Chicago, IL 60637.  
E-mail: leiw@uchicago.edu

## ABSTRACT

10 The phase speed spectrum of ocean mesoscale eddies is fundamental to our  
11 understanding of turbulent baroclinic flows. Since eddy phase propagation  
12 has been shown to modulate eddy fluxes, an understanding of eddy phase  
13 speeds is also of practical importance for the development of improved eddy  
14 parameterizations for coarse resolution ocean models. However, it is not to-  
15 tally clear whether and how linear Rossby wave theory can be used to explain  
16 the phase speed spectra in various weakly turbulent flow regimes. Using lin-  
17 ear stability analysis of the two-layer quasigeostrophic model, we identify the  
18 theoretical constraints that control the eddy phase speed. We verify these con-  
19 straints in nonlinear two-layer QG simulations, spanning a range of parame-  
20 ters with potential relevance to the ocean. We find that the strength of the  
21 inverse cascade exerts an important control on the eddy phase speed. If the  
22 inverse cascade is weak, the phase speed spectrum is reasonably well approx-  
23 imated by the phase speed of the linearly most unstable modes. A significant  
24 inverse cascade instead leads to barotropization, which in turn leads to mean  
25 phase speeds closer to those of barotropic-mode Rossby waves. Our results  
26 are qualitatively consistent with the observed eddy phase speed spectra in the  
27 Antarctic Circumpolar Current and may also shed light on the interpretation  
28 of phase speed spectra observed in other regions.

29 **1. Introduction**

30 Mesoscale eddies (on scales of tens to hundreds of km) are ubiquitous in the ocean, and are believed to be crucial in the transport of tracers and the rectification of the mean flow (e.g., Gill et al. 31 1974; Johnson and Bryden 1989; Hallberg and Gnanadesikan 2006; Mcwilliams 2008; Waterman et al. 32 2011). Yet many of their fundamental properties are still poorly understood. This contribution focusses on the question of what controls the phase speeds of mesoscale eddies, which 33 has recently been highlighted as an important factor in modulating the magnitude of eddy fluxes (e.g. Marshall et al. 2006; Ferrari and Nikurashin 2010; Abernathey et al. 2010; Klocker et al. 34 2012a; Klocker and Abernathey 2013; Bates et al. 2014). As described by the theory of Ferrari 35 and Nikurashin (2010), eddy propagation relative to the background mean flow suppresses the efficiency of eddy-driven mixing (see also Klocker et al. 2012a,b). Incorporating this effect into 36 mesoscale parameterizations may improve coarse-resolution ocean models which do not resolve 37 mesoscale fluxes (Bates et al. 2014). A deeper physical understanding of what controls eddy phase 38 speeds may help achieve this goal.

43 Observationally, remote sensing of sea-surface height (SSH), temperature, and color has provided the primary source of information about global mesoscale eddy characteristics. Several 44 different methods have been used to characterize eddy propagation speeds in these data sets. Arguably 45 the most straightforward method is to fit lines to a longitude-time Hovmöller diagram, either by eye or using a Radon transform, as first implemented by Chelton and Schlax (1996) on 46 the 3 years of Topex/Poseidon SSH data available at the time. Wavenumber-frequency spectral 47 analysis has also been used to characterize phase speeds of SSH alone (Zang and Wunsch 1999; 48 Wunsch 2009; Wortham 2013), and of the covariance between SSH, SST and ocean color (Hill 49 et al. 2000; Cipollini et al. 1997, 2001; Killworth and Blundell 2004; Abernathey and Wortham 50 51

52 2015). Fu (2009) used space-time lag-correlation to identify the eddy propagation patterns and  
53 speed. Finally, the direct tracking of individual coherent eddy features has also been implemented  
54 (Chelton et al. 2011).

55 A common feature of mesoscale eddies, as shown in the works cited above, is that over most  
56 of the ocean the observed eddy propagation is westward, except for the Antarctic Circumpolar  
57 Current (ACC) region and in western boundary current regions where Doppler shifting by the  
58 background mean flow is significant. Furthermore, frequency-wavenumber analysis reveals that,  
59 at least in some regions, energy is organized along “non-dispersive” lines (Wunsch 2009; Early  
60 et al. 2011) (i.e. all the energy appears to propagate with the same phase speed, regardless of  
61 wavenumber) - as is necessary to maintain coherent vortices (Taylor 1938; McWilliams and Flierl  
62 1979; Nof 1981).

63 Mesoscale eddies are inherently non-linear, and it is still a matter of debate to what extent their  
64 properties can be understood by linear dynamics (Chelton et al. 2007; Wunsch 2009). Neverthe-  
65 less, linear Rossby wave theory (well described in textbooks, e.g. Pedlosky 1979; Vallis 2006) is an  
66 important starting point for understanding mesoscale eddy properties, especially in regions where  
67 the flow is only weakly turbulent (Tulloch et al. 2009). It is appealing to attempt to use linear  
68 dispersion relations to describe the nonlinear mesoscale eddy phase speeds. However, as Chelton  
69 and Schlax (1996) first noted, the standard theory for freely propagating linear baroclinic Rossby  
70 waves often underestimates the observed phase speeds. Moreover, the commonly observed non-  
71 dispersive frequency-wavenumber spectra are inconsistent with the linear Rossby wave dispersion  
72 relation. The reasons for the observed deviations from the linear Rossby wave theory became a  
73 matter of intense discussion (Killworth et al. 1997; Dewar 1998; Killworth and Blundell 2003,  
74 2005, 2007; Tulloch et al. 2009). Klocker and Marshall (2014) recently argued that empirically  
75 eddy phase speeds over most of the ocean are reasonably well approximated by the long-wave limit

76 of the first baroclinic mode Rossby wave phase speed, Doppler shifted by the depth averaged mean  
77 velocity  $\bar{U}^x$ . The Doppler shifting is of particular importance in the ACC region, where it explains  
78 the transition from westward to eastward phase propagation – the advection by the strong eastward  
79 mean flow here exceeds the flow-relative westward propagation speed of baroclinic Rossby waves.

80 This paper aims to improve our understanding of eddy phase propagation by considering a model  
81 of quasi-geostrophic (QG) baroclinic turbulence. The characteristics of eddy phase propagation  
82 are analyzed in a fully nonlinear model and compared to linear theory. Using the insights from QG  
83 theory, analysis of SSH observations is also presented as a comparison. One motivation for this  
84 approach is the paper by Early et al. (2011), which demonstrated the important role of nonlinearity  
85 in the formation and propagation of coherent mesoscale eddies. That study examined the evolution  
86 of a reduced-gravity QG model with and without nonlinearity. When nonlinearity was present,  
87 coherent vortices formed and the wavenumber-frequency spectrum collapsed onto a non-dispersive  
88 line, with the phase speed given approximately by the long-wave limit of the reduced-gravity  
89 mode’s dispersion relation. The model used by Early et al. (2011), however, did not include  
90 baroclinicity in the background state, and cannot simulate the generation of eddies from baroclinic  
91 instability. Instead eddies were seeded using quasi-random initial conditions.

92 In a baroclinic flow, eddies and turbulence can arise as a result of baroclinic instability, and  
93 the linear dispersion relation becomes more complex (literally). The relevance of neutral mode  
94 baroclinic Rossby waves (which represent a true solution to the linearized equations only in the  
95 absence of baroclinicity) becomes unclear in the presence of a baroclinically unstable shear flow.  
96 Here we examine the eddy phase propagation properties of a homogeneous two layer QG model,  
97 which is arguably the simplest possible model that can generate eddies through baroclinic insta-  
98 bility. This model may be expected to reproduce some of the characteristics of eddies in the ACC  
99 region and possibly the western boundary current extensions, where eddies are generated by deep-

mode "Phillips-like" baroclinic instability (Tulloch et al. 2011). The model instead is less likely to allow for an adequate representation of the eddying flow in the subtropical regions, where we do not expect such deep-mode instability (Tulloch et al. 2011). The dominant eddies observed in these regions instead are likely either generated in remote regions, such as the eastern boundary currents (Zhai et al. 2010), or the result of an inverse energy cascade from smaller surface-trapped unstable modes (Qiu et al. 2014). The source of eddies in these regions is thus less likely to be described adequately by a homogeneous two layer model.

This paper is structured as follows. Section 2 starts with a description of the two-layer QG model and the relevant parameters. A linear stability analysis is performed to obtain the phase speeds of the unstable modes, and the results are compared to the phase speeds of neutral modes obtained in certain limit cases. In section 3, we conduct fully nonlinear simulations to explore the dependence of the eddy phase speeds and frequency-wavenumber spectra on various model parameters; the results are interpreted in terms of the linear theory discussed in section 2. We consider some general properties of baroclinic turbulence, such as the barotropization in the turbulent cascade. With this, we will argue that much of the dependence of eddy phase speeds on external parameters can be understood in terms of the linear theory. In section 4 we compare the results of the QG model to SSH observations. Conclusions are given in section 5.

## 2. Linear Analysis

This section describes the phase speed predictions that can be made based on linear analysis of the two-layer QG model.

<sup>120</sup> a. The model

<sup>121</sup> We use a two-layer QG model on a  $\beta$ -plane with a flat bottom following the formulation in Flierl  
<sup>122</sup> (1978). To place the model in an oceanic regime, we consider the two layers to have a tunable  
<sup>123</sup> layer thickness ratio  $\delta = H_1/H_2$ , where  $H_1$  and  $H_2$  are the layer thicknesses for the upper layer  
<sup>124</sup> and lower layer, respectively; for the ocean,  $\delta < 1$ . The two-layer model is forced by an imposed  
<sup>125</sup> background vertical flow shear of  $\Delta U = U_1 - U_2$  where  $U_i$  is the background zonal velocity in layer  
<sup>126</sup>  $i$ , with  $i = 1$  denoting the upper layer and  $i = 2$  denoting the lower layer.  $Q_i$  is the background  
<sup>127</sup> potential vorticity (PV) and  $q_i$  denotes the perturbation PV.

<sup>128</sup> The governing equations for the PV perturbations are:

$$\begin{aligned} \frac{\partial q_1}{\partial t} + U_1 \frac{\partial q_1}{\partial x} + \frac{\partial \psi_1}{\partial x} Q_{y1} + J(\psi_1, q_1) &= ssd \\ \frac{\partial q_2}{\partial t} + U_2 \frac{\partial q_2}{\partial x} + \frac{\partial \psi_2}{\partial x} Q_{y2} + J(\psi_2, q_2) + \frac{1}{\tau_f} \nabla^2 \psi_2 &= ssd \end{aligned} \quad (1)$$

<sup>129</sup> where the last term on the L.H.S. of the second equation denotes a linear bottom friction, with  
<sup>130</sup> a decay time scale  $\tau_f$ . The Jacobian  $J(\psi_i, q_i) \equiv \partial \psi_i / \partial x \partial q_i / \partial y - \partial \psi_i / \partial y \partial q_i / \partial x$  represents  
<sup>131</sup> nonlinear wave-wave interaction and  $ssd$  is small-scale dissipation, which will be ignored in the  
<sup>132</sup> linear analysis.

<sup>133</sup> The perturbation stream functions  $\psi_1$  and  $\psi_2$  are related to perturbation PV through the inversion  
<sup>134</sup> relation:

$$\begin{aligned} q_1 &= \nabla^2 \psi_1 + F_1(\psi_2 - \psi_1) \\ q_2 &= \nabla^2 \psi_2 + F_2(\psi_1 - \psi_2) \end{aligned} \quad (2)$$

<sup>135</sup> Similarly, the background PV gradient can be related to the vertical shear and planetary vorticity  
<sup>136</sup> gradient,  $\beta$ , via:

$$\begin{aligned} Q_{y1} &= \beta + F_1 \Delta U \\ Q_{y2} &= \beta - F_2 \Delta U \end{aligned} \quad (3)$$

<sup>137</sup> where  $F_1$  and  $F_2$  are defined as:

$$\begin{aligned} F_1 &= \frac{1}{(\delta+1)L_d^2} \\ F_2 &= \frac{\delta}{(\delta+1)L_d^2} \end{aligned} \tag{4}$$

<sup>138</sup> where  $L_d$  is the baroclinic deformation radius. The barotropic component of the streamfunction  
<sup>139</sup> ( $\psi_{BT}$ ) and the baroclinic component of the streamfunction ( $\psi_{BC}$ ) can be defined (Flierl 1978; Arbic  
<sup>140</sup> and Flierl 2004) as:

$$\begin{aligned} \psi_{BT} &= \frac{1}{1+\delta}(\delta\psi_1 + \psi_2) \\ \psi_{BC} &= \frac{\sqrt{\delta}}{1+\delta}(\psi_1 - \psi_2) \end{aligned} \tag{5}$$

<sup>141</sup> In this study, we assume a positive vertical mean flow shear (i.e. eastward), which is consistent  
<sup>142</sup> with observations over most eddy-rich regions of the world oceans.

<sup>143</sup> For instability to occur, in the absence of friction, the PV gradient must change sign between  
<sup>144</sup> the upper layer and lower layer, so as to support counter-propagating Rossby waves.  $Q_{y1}$  is always  
<sup>145</sup> larger than zero for a positive vertical mean flow shear, and thus stability is governed by the non-  
<sup>146</sup> dimensional criticality parameter:

$$\xi = \frac{F_2 \Delta U}{\beta}. \tag{6}$$

<sup>147</sup> If  $\xi > 1$  (equivalent to  $Q_{y2} < 0$ ), instability can occur in the inviscid limit.

<sup>148</sup> More generally, in the presence of friction, we can define three independent non-dimensional  
<sup>149</sup> parameters. Normalizing length scales with  $L_d$  and time scales with  $L_d/\Delta U$ , we obtain:

<sup>150</sup> 1. layer thickness ratio  $\delta$

<sup>151</sup> 2. bottom frictional damping rate  $\tau_f^{*-1} = L_d/(\Delta U \tau_f)$

<sup>152</sup> 3. nondimensional planetary vorticity gradient  $\beta^* = \beta L_d^2/\Delta U$ .

<sub>153</sub> (The asterisk denotes a non-dimension parameter.) The non-dimensional planetary vorticity gra-  
<sub>154</sub> dient is related to the criticality parameter via:

$$\xi = \frac{\delta}{(1 + \delta)\beta^*} . \quad (7)$$

<sub>155</sub> These three parameters collectively determine the basic properties of the two-layer QG model. We  
<sub>156</sub> explore different flow regimes by varying these three parameters.

<sub>157</sub> *b. Linear dispersion relations*

<sub>158</sub> In a square, doubly periodic domain, we assume a plane-wave solution:

$$\psi_i = \Re \tilde{\psi}_i e^{i(kx+ly-\omega t)} = \Re \tilde{\psi}_i e^{ik(x-ct)+ily} \quad (8)$$

<sub>159</sub> where  $k$  and  $l$  are the zonal and meridional wavenumbers, and  $\Re$  denotes the real part. Generally  
<sub>160</sub>  $c \equiv \omega/k$  is a complex number whose real part represents the zonal phase propagation speed and  
<sub>161</sub> imaginary part represents the growth/decay rate of an unstable mode. Linear solutions are obtained  
<sub>162</sub> by replacing terms in the linearized equation (1) with this plane-wave solution.

<sub>163</sub> Before considering the full linear instability problem, we first review the three neutral mode  
<sub>164</sub> solutions which arise in relevant limit cases. When the lower layer is either much deeper than  
<sub>165</sub> the upper layer, or when bottom friction is very strong, the lower layer flow becomes very weak,  
<sub>166</sub> i.e.  $\psi_2 \ll \psi_1$ . The lower layer equation in (1) then becomes a second-order equation, while the  
<sub>167</sub> linearized upper-layer equation to first order yields the reduced gravity model (considered by Early  
<sub>168</sub> et al. 2011):

$$\frac{\partial}{\partial t} (\nabla^2 \psi_1 - F_1 \psi_1) + U_1 \frac{\partial}{\partial x} (\nabla^2 \psi_1 - F_1 \psi_1) + \frac{\partial \psi_1}{\partial x} Q_{y1} = 0 . \quad (9)$$

<sub>169</sub> The dispersion relation for the reduced gravity mode is

$$c_{RG} = \frac{\omega}{k} = U_1 - \frac{Q_{y1}}{k^2 + l^2 + F_1} \quad (10)$$

<sup>170</sup> where the subscript  $RG$  means “reduced-gravity”.

<sup>171</sup> On the other hand, in the limit of vanishing vertical shear ( $\Delta U \rightarrow 0$ ) and neglecting bottom  
<sup>172</sup> friction, the eigenvalue problem posed by the linearized version of equation (1) yields two neutral  
<sup>173</sup> modes: a barotropic mode and a baroclinic mode. The dispersion relation for the barotropic mode  
<sup>174</sup> is:

$$c_{BT} = U_b - \frac{\beta}{k^2 + l^2} \quad (11)$$

<sup>175</sup> where  $U_b \equiv (\delta U_1 + U_2)/(1 + \delta)$  is the barotropic mean flow<sup>1</sup>.

<sup>176</sup> The dispersion relation for the baroclinic mode is:

$$c_{BC} = U_b - \frac{\beta}{k^2 + l^2 + 1/L_d^2} \underset{long-wave\;limit}{\approx} U_b - \beta L_d^2 \quad (12)$$

<sup>177</sup> where  $L_d$  is the deformation radius of the first baroclinic mode. The R.H.S. represents the long-  
<sup>178</sup> wave limit, which has recently been argued to provide a good fit to the eddy phase propagation  
<sup>179</sup> characteristics obtained from altimetric observations. (Tulloch et al. 2009; Klocker and Aber-  
<sup>180</sup> nathey 2013; Klocker and Marshall 2014; Abernathey and Wortham 2015)

<sup>181</sup> Comparing  $c_{BC}$  with  $c_{RG}$ , three major differences appear: (1)  $c_{BC}$  is Doppler shifted by the  
<sup>182</sup> depth-average flow, while  $c_{RG}$  is Doppler shifted by the upper layer flow. (2)  $c_{BC}$  feels the plane-  
<sup>183</sup> tary vorticity gradient  $\beta$ , while  $c_{RG}$  feels the upper layer PV gradient  $Q_{y1}$ . (3)  $c_{BC}$  feels the first  
<sup>184</sup> baroclinic deformation radius, while  $c_{RG}$  feels the upper layer deformation radius.

---

<sup>1</sup>Formally the solutions in Eqs. (11) and (12) are derived assuming  $\Delta U = 0$  and thus  $U_b = U_1 = U_2$ . There is thus some arbitrariness in the formulation of the “Doppler shift” in Eqs. (11) and (12). The formulations here were chosen such that the phase speeds remain independent of any background baroclinicity that may be present.

185    *c. Linear instability*

186    This subsection revisits the instability properties of the full two-layer QG model. Linearizing  
 187    Eq. (1) and using (2) and (8) yields:

$$\begin{pmatrix} -(U_1 - c)(k^2 + l^2 + F_1) + Q_{y1} & (U_1 - c)F_1 \\ (U_2 - c)F_2 & -(U_2 - c)(k^2 + l^2 + F_2) + Q_{y2} + \frac{i}{k\tau_f}(k^2 + l^2) \end{pmatrix} \begin{pmatrix} \psi_1 \\ \psi_2 \end{pmatrix} = 0 \quad (13)$$

188    For non-trivial solutions, the determinant of coefficients must be zero. This provides a quadratic  
 189    equation for  $c$ , which yields two solutions. In the absence of bottom friction a pair of complex  
 190    conjugate solutions are obtained for baroclinically unstable mean shears ( $\xi > 0$ ), denoting one  
 191    growing and one decaying mode.

192    We now review the impact of nonzero friction on the linear stability analysis. The inclusion of  
 193    friction affects both growth rates and phase speeds. In the upper panel of Fig. 1, we show numer-  
 194    ical solutions for the growth rate using parameters roughly characteristic of the ACC:  $\delta = 0.25$ ,  
 195     $\Delta U = 0.04 \text{ m/s}$  and  $L_d = 15 \text{ km}$ . The layer depth ratio of 0.25 is roughly consistent with the depth  
 196    of the sign-reversal in the observed extra-tropical zonal-mean QGPV gradient (Tulloch et al. 2011).  
 197    Similarly, the vertical shear and deformation radius are in rough agreement with observations in  
 198    the ACC region. We will return to a more quantitative comparison between the QG model and  
 199    the observations in section 4. In these linear solutions, the meridional wavenumber  $l$  is set to be  
 200    zero, leading to the fastest possible growth rate (the standard textbook approach, e.g. Vallis 2006).  
 201    In the following sections, we will also discuss the solutions in which the meridional wavenumber  
 202     $l$  is set to be identical to zonal wavenumber  $k$ , as ocean observations suggest that the zonal and  
 203    meridional wavenumbers are generally of similar order.

204    When friction is absent, both a short-wave cutoff and long-wave cutoff can be identified. How-  
 205    ever, with increasing frictional strength, the short waves and some long waves are destabilized

206 while maximum growth rates decrease. The length scale of the most unstable modes also slightly  
207 decreases with increasing frictional strength. The lower panel in Fig. 1 shows the phase speed.  
208 Unstable modes propagate eastward ( $\Re(c) > 0$ ) at most wavelengths. Only when friction is weak,  
209 the phase speed can be slightly westward ( $\Re(c) < 0$ ). Once the frictional damping time-scale is  
210 below about 40 days, the effect of friction on the phase speed becomes relatively weak.

211 The dispersion curves for the reduced gravity mode (dashed) and the barotropic mode (dot-  
212 dashed) are also plotted in the lower panel of Fig. 1. The phase speeds of the linearly unstable  
213 modes consistently fall between these two neutral curves but are generally quite close to that of  
214 the reduced gravity mode, particularly in the limit of strong friction. Since  $c_{RG}$  represents the  
215 limit of strong stratification and strong friction,  $c_{RG}$  is not very different from the full two-layer  
216 unstable mode dispersion relation when the layer thickness ratio is relatively small and friction  
217 is significant. In fact, it appears that (10) is quite effective at predicting the phase speed of the  
218 unstable modes without solving the full instability problem. Notice, that the reduced-gravity curve  
219 represents the limit where the streamfunctions in the two layers upper layer is fully decoupled due  
220 to the strong lower layer friction, whereas the barotropic curve represents the opposite limit, where  
221 the streamfunctions in both layers are identical.

222 The baroclinic dispersion curve  $c_{BC}$  is also plotted in the lower panel of Fig. 1 for comparison.  
223 The baroclinic mode phase speed shows a relatively weak wavenumber dependence, and is less  
224 clearly related to the full linear instability problem; although the overall phase speed is close to that  
225 of the fastest growing modes. Whether the agreement between the baroclinic mode phase speed  
226 and the phase speed of the fastest growing mode is a coincidence or is driven by some physical  
227 mechanism remains unclear.

228 Notice that  $c_{BC}$  and  $c_{RG}$  are not always easy to distinguish in the real ocean. For example, in  
229 the sub-tropical gyres, the first baroclinic mode typically becomes strongly surface intensified –

corresponding to an upper layer that is much shallower than the lower layer. The upper layer deformation radius in  $c_{RG}$  then is well approximated by the first baroclinic deformation radius as in  $c_{RG}$ . Moreover, the vertical shear is typically weak, such that the upper-ocean PV gradient in  $c_{BC}$  approximately reduces to the planetary vorticity gradient as in  $c_{RG}$ , and Doppler shifting by the barotropic flow becomes indistinguishable from Doppler shifting by the upper-ocean flow. On the other hand, in other regions, such as the ACC, the differences between  $c_{BC}$  and  $c_{RG}$  should be more pronounced.

### 3. Nonlinear Model

The linear analysis described above reveals the phase speeds of linear modes. However, in a nonlinear equilibrated state, it is not *a priori* clear which wavenumbers get energized and whether the eddies in the nonlinear flow actually follow a linear dispersion relation. This section presents frequency-wavenumber spectra and phase speed spectra from a series of nonlinear two-layer QG simulations and compares them to the predictions from linear theory.

#### a. Model description and methods

We numerically solve the fully nonlinear two-layer QG model described by equation (1). We use a doubly periodic domain with a horizontal resolution of  $256 \times 256$  grid points in real space. Enstrophy is removed near the grid scale with an exponential filter which is identical to that described in Arbic and Flierl (2004).

The parameters in the control simulation are as in the linear analysis discussed in section 2:

$$L_d = 15 \text{ km} , U_1 = 0.04 \text{ m/s} , U_2 = 0 \text{ m/s} , \tau_f = 20 \text{ days} , \delta = 0.25 . \quad (14)$$

The frictional decay rate of  $(20 \text{ days})^{-1}$  is empirically chosen to obtain eddy properties that are roughly consistent with observations in the ACC region. Determination of a realistic frictional

time scale from first principles is not straightforward, as it crudely represents various routes to dissipation near the bottom boundary (see also Arbic and Flierl 2004). The positive mean flow vertical shear of  $0.04 \text{ m/s}$  is consistent with observations in the ACC region. The parameters in our two-layer QG model correspond to a non-dimensional criticality parameter of  $\xi \approx 2.37$ , which is moderately supercritical.

As a case study, we present three reference simulations. These three simulations use the above listed parameters but with different frictional strengths. In addition to the control run which uses  $\tau_f = 20 \text{ days}$ , the strong friction run and the weak friction run use  $\tau_f = 10 \text{ days}$  and  $\tau_f = 40 \text{ days}$ , respectively. In Fig. 2, the Hovmöller diagram of the upper layer streamfunction in the control run suggests no clear preferential direction of propagation. Comparing all three simulations in Fig. 2 suggests that decreasing the frictional strength to  $(40 \text{ days})^{-1}$  enhances westward propagation; while increasing the frictional strength to  $(10 \text{ days})^{-1}$  arguably favors eastward propagation.

In addition to the three reference simulations, to comprehensively examine the phase speeds in the two-layer QG model, we conduct several groups of experiments, each varying only one non-dimensional parameter. All groups include more than 20 simulations to explore each non-dimensional parameter spanning over 2 orders of magnitude.

1. In the experiments dubbed THIC, the layer thickness ratio  $\delta$  is varied, while  $\tau_f^*$  and  $\beta^*$  are held fixed.
2. In the FRIC experiments,  $\tau_f^*$  is varied, while  $\delta$  and  $\beta^*$  are held fixed.
3. In the BETA experiments,  $\beta^*$  is varied, while  $\delta$  and  $\tau_f^*$  are held fixed. The additional group BETA-hf is similar to the BETA experiments, but with strong frictional strength.

Among all simulations, the output data of the first 10 years is dropped, and streamfunction snapshots for both layers from the following 50 years are sampled every 5 days.

274 Analysis of the nonlinear simulations is based on spectral analysis in wavenumber and frequency  
 275 space (Hayashi 1971). The streamfunction  $\psi_i(x, y, t)$  is Fourier-transformed into spectral space as  
 276  $\hat{\psi}_i(k, l, \omega)$ , where  $k$ ,  $l$ , and  $\omega$  are zonal wavenumber, meridional wavenumber, and frequency,  
 277 respectively. Fig. 3 shows the upper-layer eddy kinetic energy as a function of zonal and merid-  
 278 ional wavenumber,  $E_1(k, l)$ , for our three reference simulations. The EKE as a function of zonal  
 279 and meridional wavenumber can be obtained from the three-dimensional streamfunction variance  
 280 spectrum by multiplication with the total wavenumber and integration over all frequencies,  $\omega$ :

$$E_i(k, l) = \int \frac{1}{2} (k^2 + l^2) |\hat{\psi}_i(k, l, \omega)|^2 d\omega \quad (15)$$

281 The EKE is nearly isotropic for all three reference simulations. The parameters considered here  
 282 evidently do not give rise to multiple-jet-formation regimes (Rhines 1975; Maltrud and Vallis  
 283 1991). Because of the isotropic behavior in our model, and the focus on zonal phase propaga-  
 284 tion, our frequency-wavenumber analysis will focus on the dependence on frequency and zonal  
 285 wavenumber,  $k$ . Rather than showing total EKE as a function of zonal wavenumber, we will more-  
 286 over focus on the meridional velocity variance spectra, which can be obtained by integrating the  
 287 streamfunction variance spectrum over all zonal wavenumbers and multiplying by  $k^2$ :

$$E_{\perp i}(k, \omega) = k^2 \int \frac{1}{2} |\hat{\psi}_i(k, l, \omega)|^2 dl \quad (16)$$

288 The zonal spectrum of meridional velocity (i.e. the “cross-track” velocity spectrum) has the  
 289 advantage that it better picks up the peak in the EKE spectrum, as compared to a zonal EKE  
 290 spectrum that includes the “along-track” velocity component (Wortham et al. 2014). The cross-  
 291 track spectrum further has the advantage that it is more trivially related to the streamfunction  
 292 variance spectrum, as the  $k^2$  is outside of the integral in equation (16). Finally, it is the meridional  
 293 eddy velocity which is typically most important for the transport of heat and tracers in the ocean  
 294 (Klocker and Marshall 2014; Abernathey and Wortham 2015).

295    *b. General Results*

296    In this section, we discuss the general characteristics of the turbulent flow fields in the fully  
297    nonlinear two-layer QG simulations, and explore the dependence of the eddy properties on the  
298    three non-dimensional parameters. Linear theory highlights the different propagation behavior  
299    of the barotropic and baroclinic modes, so this decomposition is a useful starting point for our  
300    analysis of the nonlinear simulations. Using equation (5), we can separate the energy spectra into  
301    barotropic and baroclinic components. Fig. 4 shows the ratio of barotropic mode EKE to total EKE  
302    as a function of zonal wavenumber. This ratio is bigger toward small wavenumbers in the control  
303    experiment, indicating a trend towards enhanced barotropitization at larger scales. Comparing  
304    all three reference simulations, the barotropitization is enhanced when friction is weak, and vice  
305    versa. This is consistent with our understanding of the inverse cascade in QG turbulence (Salmon  
306    1980).

307    In Fig. 5, we show the parameter dependence of the ratio of barotropic EKE to total EKE by av-  
308    eraging over all horizontal wavenumbers and frequencies, in all simulations in THIC, FRIC, BETA  
309    and BETA-hf. The flow becomes more barotropic when (1) layer thickness ratio approaches unity,  
310    (2) friction is reduced, (3)  $\beta^*$  is reduced. All of these dependencies are in qualitative agreement  
311    with previous results (e.g. Arbic and Flierl 2004). In the simulations whose total EKE is dominated  
312    by the barotropic mode, we might expect the dispersion relation of the barotropic mode to provide  
313    a better prediction of the eddy phase speeds. We will test this hypothesis in the next subsection.

314    In addition to barotropitization, non-linear eddy-eddy interactions tend to lead to an increase  
315    in the horizontal eddy scale, beyond the scale of the most unstable mode. To characterize length  
316    scales, we integrate the power spectra over all frequencies to obtain a univariate zonal wavenumber  
317    spectrum for each experiment. Furthermore, the spectral energy budget at the zonal wavenumber

318  $k$  can be written as below, following the formalisms in Jansen and Held (2014):

$$\partial_t E_k = S_k + TA_k + TK_k - F_k - V_k \quad (17)$$

319 Here,  $E_k$ ,  $S_k$ ,  $TA_k$ ,  $TK_k$ ,  $F_k$ ,  $V_k$  represent total kinetic energy for both layers, the extraction of  
320 available potential energy (APE) from the prescribed background state, spectral transfer of APE,  
321 spectral transfer of kinetic energy, frictional dissipation by bottom drag, and small scale dissipa-  
322 tion, respectively.

323 The sum of  $S_k$  and  $TA_k$  is the conversion from available potential energy to eddy kinetic energy.

324  $S_k$  and  $TA_k$  can be calculated through

$$S_k = \frac{U}{L_d^2} \Re[ik \widehat{\psi_{BT}} \widehat{\psi_{BC}}^*]_k \quad (18)$$
$$TA_k = -\frac{1}{L_d^2} \Re[\widehat{\psi_{BC}}^* J(\widehat{\psi_{BT}}, \widehat{\psi_{BC}})]_k$$

325 where the asterisk denotes the complex conjugate, and  $(\widehat{\dots})$  denotes the Fourier transform, here  
326 with respect to zonal wavenumber.

327 In Fig. 6, we use the diagnosed spectra of net conversion from APE to EKE (top row) to indicate  
328 the scale at which kinetic energy is injected into the system. The peak in the conversion spectrum  
329 roughly coincides with the peak in the linear growth rate, which is shown in the bottom row.  
330 The departure between the peak in the conversion spectrum and the peak in the barotropic EKE  
331 spectrum gives an indication of the inverse cascade range.

332 The THIC experiments (first column) show that simulations with equal layer depths exhibit a  
333 slightly enhanced inverse cascade compared with simulations with a shallower upper layer. The  
334 FRIC experiments (second column) exhibit the most significant changes in the inverse cascade  
335 range, with a strong inverse cascade found in limit of weak friction, consistent with Arbic and  
336 Flierl (2004). This robust inverse cascade is a signature of strong nonlinear eddy-eddy interac-  
337 tions. In the weak friction limit, there is no direct correspondence between the most unstable

338 wavenumbers and the energy containing wavenumbers; linear stability analysis only predicts the  
339 injection scale. The BETA and BETA-hf experiments show that the energy cascade range is re-  
340 duced for large  $\beta^*$ , which is in agreement with the general understanding that the beta-effect limits  
341 the inverse energy cascade (Rhines 1979). However, for small  $\beta^*$  the halting scale converges to a  
342 constant value, which again depends on the bottom friction (compare the third and fourth columns  
343 in Fig. 6).

344 In summary, although all non-dimensional parameters influence the strength of the inverse cas-  
345 cade, it is here found to be most sensitive to the frictional strength. Many theoretical arguments  
346 have been developed to predict the halting scale of the inverse energy cascade (e.g. Rhines 1979;  
347 Held and Larichev 1996; Arbic and Flierl 2004; Thompson and Young 2007; Jansen et al. 2015).  
348 However, our focus here is on the eddy phase speed, and a detailed comparison between inverse  
349 cascade strength and different scaling laws is beyond the scope of this contribution.

### 350 c. Phase Speed Spectra

351 To characterize zonal phase speeds in the nonlinear simulations, we now consider the  
352 wavenumber-frequency spectrum, which can be compared to the linear dispersion relationships  
353 discussed in section 2. To further quantify the dominant phase speed, the wavenumber-frequency  
354 spectrum can be transformed to a wavenumber-phase-speed spectrum, following Randel and Held  
355 (1991) (see also Abernathey and Wortham 2015). The top row in Fig. 7 shows the wavenumber-  
356 frequency cross-track EKE ( $E_{\perp}$ ) spectra for our three reference cases: the control run, the weak  
357 friction case, and the strong friction case. Since  $E_{\perp}$  is proportional to  $k^2$  times the stream-function  
358 variance (Eq. 16), the  $E_{\perp}$  spectra by construction vanish in the limit of vanishing zonal wavenum-  
359 ber and highlight the wavenumber range of the energy-containing eddies. To make a connection  
360 between  $E_{\perp}$  spectra and the streamfunction spectra often considered in the oceanographic litera-

ture (e.g. Wunsch 2009), and to investigate the dispersion relation at all zonal wavenumbers, the middle row of Fig. 7 shows the wavenumber-frequency spectra normalized by the total power at each zonal wavenumber. Finally, the bottom row shows the interpolated wavenumber-phase-speed spectra of  $E_{\perp}$  (without any normalization).

To facilitate the comparison with linear theory, the dispersion relations discussed in Sec. 2 are also plotted in Fig. 7. Focussing first on the normalized frequency-wavenumber spectrum of the control experiment (middle panel of the middle row of Fig. 7), we find that the barotropic dispersion curve  $\omega_{BT}$  and the reduced-gravity curve  $\omega_{RG}$  overlap with different energy-containing regions of the power spectrum— $\omega_{BT}$  agrees better with the low-frequency part the spectrum, whereas  $\omega_{RG}$  traces the high-frequency, high-wavenumber end of the spectrum. In comparing the three simulations, as frictional strength varies from strong to weak, the maximum of the raw frequency-wavenumber  $E_{\perp}$  spectrum (top row of Fig. 7) shifts from positive frequency toward negative frequency. Correspondingly, in the phase speed spectra (bottom row of Fig. 7) the predominant phase speed shifts from eastward to westward when friction is varied from strong to weak values. The peak of the energy spectrum generally falls roughly within the region enclosed by the two neutral dispersion curves  $\omega_{BT}$  and  $\omega_{RG}$ . The phase speed of the baroclinic mode in its long-wave limit (proposed as a predictor of eddy phase speeds by Klocker and Marshall (2014)) agrees reasonably well with the energy peak in the control run and the strong friction run, but does not capture the fast westward propagation at weak friction. The faster westward propagation at weak friction is qualitatively consistent with the increased inverse energy cascade (Fig. 6) and barotropization (Fig. 5).

In all these panels, for both  $C_{RG}$  and  $C_{BT}$ , the dashed curves assuming isotropic eddies (i.e.  $l = k$ ) slightly differ from the solid curves which assume  $l = 0$ , although the solutions don't differ qualitatively. For  $C_{RG}$ , the  $l = k$  curves tend to be more consistent with the energy peak, whereas

385 for  $C_{BT}$  the  $l = 0$  curves tend to be more consistent with the energy peak. This difference may  
386 be indicative of varying degrees of eddy anisotropy, but it may also simply be an artifact of the  
387 projection of the three-dimensional  $\omega - k - l$  spectra onto two-dimensional  $\omega - k$  spectra.

388 To examine how phase speeds vary in the THIC, FRIC, BETA and BETA-hf experiments, we  
389 integrate the wavenumber-phase-speed spectra over all horizontal wavenumbers, producing a one-  
390 dimensional phase speed spectrum for each experiment. In Fig. 8, the top row shows the diagnosed  
391 phase speed spectra from all nonlinear simulations in the THIC, FRIC, BETA and BETA-hf series,  
392 and the bottom row shows the growth rate as a function of phase speed from the linear stability  
393 analysis. For easy comparison, the general structure of Fig. 8 is similar to that of Fig. 6. The  
394 aforementioned three dispersion relation curves  $C_{RG}$ ,  $C_{BT}$  and  $C_{BC}$  (long-wave limit) in Sec. 2 are  
395 plotted on top of each panel for comparison. The calculation of  $C_{RG}$  and  $C_{BT}$  for each simula-  
396 tion requires a specified zonal wavenumber, which we identify as the inverse centroid of the  $E_\perp$   
397 spectrum.

398 We first focus on the effect of varying layer thickness ratio in the THIC experiments (left col-  
399 umn of Fig. 8). For shallow upper layer (small  $\delta$ ), the EKE-containing eddies propagate eastward,  
400 which is close to the linear prediction from baroclinic instability analysis (bottom row). For mod-  
401 erately shallow upper layer ( $\delta \approx 10^{-1}$ ), the reduced-gravity curve  $C_{RG}$  captures the peak of the  
402 phase speed reasonably well. In the equal layer depth limit ( $\delta \approx 10^0$ ), the phase speed of the  
403 barotropic mode arguably captures the peak of  $E_\perp$  spectrum best. We also see an increase in  
404 the spread of the phase speed spectrum with increased layer depth ratio, which is indicative of  
405 increased turbulence leading to the dominance of chaotic advection.

406 We next focus on the role of varying the non-dimensional planetary vorticity gradient in the  
407 BETA and BETA-hf experiments (right two columns of Fig. 8). For strong non-dimensional beta  
408 (marginal criticality), the most energetic eddies generally propagate eastward, consistent with the

eastward propagation of the linearly most unstable modes. As  $\beta^*$  is reduced (criticality increases), the peak of the eddy phase speed spectrum in BETA shifts slightly westward and then back eastward, while the peak of the eddy phase speed spectrum in BETA-hf does not change much across the entire parameter space. In the BETA experiments, as  $\beta^*$  is reduced, there exist two parameter regimes: First, reducing the non-dimensional beta leads to barotropization, which leads to more westward phase propagation as eddies approach the phase speed of the barotropic mode. As  $\beta^*$  is further reduced, the barotropic mode phase speed itself becomes weaker and eventually turns eastward. In the BETA-hf experiments, on the other hand, friction suppresses barotropization and the phase speed remains better approximated by the reduced gravity mode through the entire range of  $\beta^*$ . In both the BETA and (to a lesser degree) BETA-hf experiments, we also see an increase in the spread of the phase speed spectrum with decreasing  $\beta^*$ . This is consistent with theoretical predictions, as the more supercritical mean state is expected to lead to more vigorous turbulence (e.g. Held and Larichev 1996).

By and large, varying the layer thickness ratio and non-dimensional beta does not change the peak of the phase speed spectrum substantially. However, in the FRIC experiments (second column in Fig. 8), when friction becomes weaker, the predominant phase speed shifts significantly from eastward propagation to fast westward propagation. In the weak friction regime, the peak of the phase speed spectrum is well captured by the barotropic neutral dispersion relation curve, and is far away from the predictions of linear stability analysis (compare to the second row). As shown in Fig. 6 and Fig. 5, the weak friction regime is characterized by a robust inverse energy cascade and barotropization, indicating that non-linear eddy-eddy interactions are the main reason for the departure of the eddy phase speeds from linear stability predictions. In spite of the strong non-linearity in the weak friction limit, the linear barotropic-mode dispersion relation provides a good predictor for the eddy phase speeds, given the energy containing wavenumber. The baroclinic and

433 barotropic modes were also analyzed separately (not shown) and were found to have very similar  
434 spectra, indicating tight coupling between modes.

435 We conclude that in the two-layer model, the strength of the inverse cascade determines the  
436 eddy length scale and amount of barotropization, which in turn determines the predominant eddy  
437 phase speed. When the flow is largely concentrated in the upper-layer (e.g. due to strong bottom  
438 friction), the reduced-gravity dispersion curve  $c_{RG}$  is more apt, whereas when the flow is largely  
439 barotropic, the barotropic dispersion curve  $c_{BT}$  gives a better estimate.

## 440 4. Observations

441 In this section, we explore spatial-temporal spectral analysis of satellite observations and com-  
442 pare them to the QG model results discussed in the previous sections. The point of this exercise  
443 is to reveal which aspects of observed eddy propagation can and cannot be explained in terms of  
444 the physical arguments given above. We focus on two qualitatively different regions. The South-  
445 ern Ocean, especially around the Antarctic Circumpolar Current (ACC), may share some essential  
446 properties with the two-layer QG model. On the other hand, the subtropics are characterized  
447 by more “non-dispersive” eddies (Wunsch 2009), and a shallow-mode instability that is not well  
448 represented by the two-layer QG model (Tulloch et al. 2009).

### 449 a. Data

450 We use 22 years of gridded geostrophic velocity anomalies and absolute geostrophic velocities  
451 produced by the SSALTO/DUACS multimission altimeter processing system and distributed by  
452 AVISO. Since the focus of this study is on the extra-tropical region, where the assumption of  
453 geostrophy is largely valid, we expect the AVISO products to reasonably reflect the underlying  
454 flow field. The grid size of AVISO is  $0.25^\circ$ , which in the ACC region corresponds to around 15

455 km. Low-pass Lanczos filtering has been applied to the product during the gridding procedure to  
456 remove the residual noise and small scale signals below 65 km globally. Since in this study we  
457 focus on mesoscale eddies, which typically are larger than 200 km (Stammer 1997), the 65 km  
458 cutoff scale of the filter should not bias our core results, though some caution must be used in the  
459 interpretation of the data at higher wavenumbers.

460 For comparison with the two-layer QG model, the ideal testbed in observations should have a  
461 homogeneous background flow and relatively small topographic effect on the eddies. We choose  
462 two regions with relatively flat topography and homogeneous background flow in a subtropical  
463 region and the ACC, respectively. The subtropical region is in the northeast Pacific at  $27.625^{\circ}$   
464 N from  $180^{\circ}$ W to  $140^{\circ}$ W, identical to that discussed in Wunsch (2009) (hereafter referred to as  
465 Wunsch region). The ACC region is at  $57.625^{\circ}$  S in the southeast Pacific from  $117.375^{\circ}$ W to  
466  $77.375^{\circ}$ W. Fig. 9 shows the climatological zonal component of the absolute geostrophic velocities  
467 for the two chosen regions, averaged for the year 2012. Both these regions are characterized by  
468 zonally homogeneous mean flow. The ACC region is at the core of the ACC and has a climato-  
469 logical zonal surface mean flow much stronger than the zonal surface mean flow in the Wunsch  
470 region.

471 *b. Methods*

472 To compare the observations with the results inferred from the two-layer QG model, we need  
473 to match the observed mean flow and stratification profiles to the relevant parameters in the QG  
474 model. A recipe for this procedure has been developed by Flierl (1978) based on a vertical mode  
475 decomposition. If the flow in the continuously stratified fluid is dominated by the barotropic and  
476 first baroclinic mode, we can construct an analog two-layer model which adequately reproduces  
477 the dynamics of these two modes.

478 The first-baroclinic-mode structure of the continuously stratified QG equations provides a con-  
 479 straint to estimate the layer thickness ratio in the two-layer QG analogue, through the relation  
 480 (Flierl 1978):

$$\delta = \frac{1}{4} [\sqrt{\xi_{111}^2 + 4} - \xi_{111}]^2, \quad (19)$$

481 where the nonlinear baroclinic self-interaction,  $\xi_{111}$ , is determined based on the first baroclinic  
 482 mode structure,  $\Phi_1(z)$ , as  $\xi_{111} = 1/H \int_{-H}^0 \Phi_1^3(z) dz$ .

483 Following Tulloch et al. (2009), based on the vertical buoyancy profile,  $N(z)^2$ , we calculate the  
 484 first eigenmode structures,  $\Phi_i(z)$ , (right panel in Fig. 10) and eigenvalues,  $K_d$ , from the Sturm-  
 485 Liouville equation:

$$\frac{d}{dz} \left( \frac{f^2}{N^2(z)} \frac{d\Phi}{dz} \right) = -K_d^2 \Phi, \quad (20)$$

486 where the buoyancy-frequency profile  $N^2(z)$  is estimated from the neutral density data in Gouretski  
 487 and Koltermann (2004) at the two chosen regions (left panel in Fig. 10). The right panel of Fig. 10  
 488 shows the first baroclinic mode in the two regions. In the ACC, it has a deep structure, and a  
 489 deformation radius of 16 km. The equivalent layer thickness ratio is found to be  $\delta \approx 0.48$ . On  
 490 the other hand, the first baroclinic mode in the Wunsch region is more surface-intensified, with a  
 491 radius of deformation of 42 km and an equivalent layer thickness ratio  $\delta \approx 0.24$ .

492 Fig. 10 shows the vertical structure of the climatological zonal-mean zonal current in the Wunsch  
 493 and ACC regions. The mean flow for the Wunsch region is taken from the ECCO state estimate  
 494 (Wunsch and Heimbach 2007), while the mean flow in the ACC is taken from the Southern Ocean  
 495 State Estimate (Mazloff et al. 2010). In the ACC, almost all zonal mean KE projects onto the  
 496 barotropic mode and first baroclinic mode (blue and black curves in Fig. 10). This projection  
 497 corresponds to a vertical mean flow shear of 3.7 cm/s in the two-layer QG analogue, on the same  
 498 order as the vertical mean flow shear considered in our QG two-layer reference setup in section 2

499 and 3. Therefore the baroclinic instability in the ACC region is expected to be dominated by deep  
500 “Phillips-type” instabilities, consistent with the findings of Tulloch et al. (2011).

501 In the Wunsch region, the projection on the two-layer QG model gives a mean state with a  
502 vertical mean flow shear of 0.24 cm/s, sub-critical to two-layer QG-type baroclinic instability  
503 in the absence of friction, suggesting that eddies in this region are either generated non-locally  
504 or arise from instabilities of higher vertical modes. Two-layer QG dynamics in this region is  
505 insufficient to directly generate baroclinic eddies, but the two-layer QG dynamics might still be  
506 relevant to interpret the local behavior of eddies that may have been generated elsewhere or through  
507 higher-mode instabilities (so long as the surface EKE is dominated by the barotropic and first  
508 baroclinic mode). In particular, in regions with weak vertical shear, such as the Wunsch region,  
509 the neutral reduced-gravity mode may be relevant for predicting eddy phase speeds (e.g. Early  
510 et al. 2011).

511 *c. Phase speed spectra*

512 Fig. 11 shows a Hovmöller diagram of surface geostrophic velocity anomalies in the two regions.  
513 Visual inspection suggests that eddies in the Wunsch region propagate predominantly westward at  
514 a relatively coherent phase speed. In the ACC region eddies propagate predominantly eastward,  
515 though it is less straightforward to identify one particular phase speed directly from the Hovmöller  
516 diagram. Instead, eddies seem to propagate at a range of different phase speeds. To quantify the  
517 phase speed spectra in the two regions, we apply the same spectral analysis as for the numerical  
518 simulations discussed in section 3. To reduce noise, the 21 years and 10 months of data is divided  
519 into 10 overlapping subsets, tapered by a Hanning window.

520 Fig. 12 is analog to Fig. 7 in the discussion of the model results. The upper row shows the  
521 wavenumber-frequency power spectrum for the meridional component of the geostrophic velocity

522 anomalies in the selected regions. The middle row shows the same spectra, but normalized at each  
523 zonal wavenumber, while the last row shows the cross-track EKE spectrum re-mapped into phase  
524 speed-wavenumber space. The neutral dispersion curves derived in section 2 are plotted on top of  
525 the spectra, with the two-layer model parameters chosen as described above.

526 The overall eddy scales for the ACC region ( $\sim 0.025 - 0.004$  cpkm) are slightly larger than the  
527 most energetic scales in our control two-layer QG simulation ( $\sim 0.003 - 0.005$  cpkm). This dif-  
528 ference is most likely attributable to the specific choice of parameters in the simulations, though  
529 shorter wavelengths may also be somewhat under-represented in the AVISO data, due to the spa-  
530 tial smoothing. In the Wunsch region, the normalized cross-track EKE spectrum (middle panel)  
531 shows robust non-dispersive behavior which is consistent with the power spectrum of sea surface  
532 elevation shown in Fig. 8 of Wunsch (2009). On the other hand, the raw cross-track EKE spectrum  
533 (upper panel) shows that the energy-containing eddies mostly fall on the high-wavenumber and -  
534 frequency limit of the non-dispersive line identified by Wunsch (2009). Interestingly, the phase  
535 speed spectrum (lower panel) of these energy-containing eddies does indicate some systematic  
536 variation in the phase speed with eddy scale, with most of the energy falling near the barotropic  
537 dispersion curve.

538 In the ACC region, the cross-track EKE spectrum exhibits dispersive behavior across a wide  
539 range of length scales. Consistent with the results from our two-layer QG simulations, both the raw  
540 and normalized cross-track EKE power spectra are concentrated roughly near the region enclosed  
541 by the dispersion relation curves of the reduced gravity mode and the dispersion relation curve  
542 of the barotropic mode. This resembles the control case in the reference simulations (compare to  
543 Fig. 7).

544 In both regions, the eddy-kinetic-energy-containing part of the phase-speed spectrum falls near  
545 the barotropic dispersion curve (bottom row in Fig. 12). The reduced-gravity mode instead best

546 approximates the dispersion relation of the largest-scale features, as best identified in the nor-  
547 malized spectra (middle row in Fig. 12). In both regions the peak in the energy spectra is also  
548 reasonably well approximated by the long-wave limit of the reduced gravity mode. The latter  
549 generally provides a better estimate than the long-wave limit of the baroclinic phase speed, which  
550 has been used in the past to fit eddy phase speeds (e.g. Klocker and Marshall 2014). Interestingly,  
551 as in many of the simulations, the intersection point between the long-wave limit of the reduced  
552 gravity mode and the barotropic mode here appears to give a reasonably good estimate of the peak  
553 in the cross-track EKE spectrum. Whether this is largely a coincidence or indicative of a physical  
554 mechanism deserves further investigation. It has previously been noted that the vertical structure  
555 of ocean eddies is often approximately equivalent barotropic, and lying between the barotropic  
556 and reduced gravity limits (e.g. Wunsch 1997; Arbic and Flierl 2004; Wortham 2013; Jansen et al.  
557 2015). The eddy phase speeds seem to support this notion.

558 We reemphasize that we do not mean to suggest that the true frictional drag in the ACC region  
559 is similar to the relatively large value used in the control reference simulation (i.e.  $20 \text{ day}^{-1}$ ). In  
560 the two-layer QG model, frictional strength is a parameter for tuning the strength of the inverse  
561 cascade. In fact, in the two-layer QG model, friction is the only parameter that can be modi-  
562 fied without affecting the other two non-dimensional parameters. The two-layer QG model lacks  
563 many other elements that can influence the inverse cascade and barotropization in the real ocean,  
564 such as bottom topography and deep stratification. The net effect of all these factors collectively  
565 determines the strength of the inverse cascade and barotropization.

## 566 5. Conclusion

567 Our results suggest that, given the degree of barotropization and the eddy length scale, linear the-  
568 ory remains relevant to understand eddy phase speeds in a fully nonlinear context. However, both

569 numerical simulations and observational analysis suggest that the simple picture of coherent eddy  
570 phase propagation at the the long-wave baroclinic Rossby-wave phase speed may be somewhat  
571 too idealized.

572 In a two-layer QG model, the eddy phase speeds can be understood largely in terms of the  
573 reduced gravity mode and barotropic mode, which represent two relevant limit cases. If the inverse  
574 cascade is weak, the phase speed spectrum is reasonably well approximated by the phase speed of  
575 the linearly most unstable mode, which in turn can be approximated by the reduced gravity mode  
576 dispersion relation. A significant inverse cascade instead leads to barotropization, which in turn  
577 leads to phase speeds closer to those of barotropic-mode Rossby waves.

578 Analysis of satellite sea surface height observations suggests that mesoscale eddy phase speeds  
579 in the ACC and Subtropics also fall within this theoretically predicted range. In the subtropics,  
580 long waves fall on non-dispersive lines as documented in Wunsch 2009, but phase speeds of the  
581 most energetic mesoscale eddies also agree with the barotropic dispersion relation. In the ACC  
582 region, the wavenumber-frequency spectra qualitatively resembles those found in the QG model.  
583 Again, the most energetic eddies mostly fall near the barotropic dispersion curve, while longer  
584 wavelengths are better approximated by the reduced gravity mode.

585 *Acknowledgments.* Much of this work was carried out at the 2014 Geophysical Fluid Dynam-  
586 ics Summer School while L.W. was a visiting student at Woods Hole Oceanographic Institution.  
587 M.F.J. and R.P.A acknowledge support from the GFD program. We thank Glenn Flierl, William  
588 Young, Rui Xin Huang, and Isaac Held for helpful comments and discussions.

589    **References**

- 590    Abernathey, R., J. Marshall, M. Mazloff, and E. Shuckburgh, 2010: Enhancement of mesoscale  
591    eddy stirring at steering levels in the southern ocean. *Journal of Physical Oceanography*, **40** (1),  
592    170–184.
- 593    Abernathey, R., and C. Wortham, 2015: Phase speed cross spectra of eddy heat fluxes in the  
594    pacific. *Journal of Physical Oceanography*.
- 595    Arbic, B. K., and G. R. Flierl, 2004: Baroclinically unstable geostrophic turbulence in the limits  
596    of strong and weak bottom ekman friction: Application to midocean eddies. *Journal of Physical*  
597    *Oceanography*, **34** (10), 2257–2273.
- 598    Arbic, B. K., K. L. Polzin, R. B. Scott, J. G. Richman, and J. F. Shriver, 2012: On eddy viscosity,  
599    energy cascades, and the horizontal resolution of gridded satellite altimeter products\*. *Journal*  
600    *of Physical Oceanography*, **43** (2), 283–300.
- 601    Bates, M., R. Tulloch, J. Marshall, and R. Ferrari, 2014: Rationalizing the spatial distribution of  
602    mesoscale eddy diffusivity in terms of mixing length theory. *Journal of Physical Oceanography*,  
603    **44** (6), 1523–1540.
- 604    Chelton, D. B., and M. G. Schlax, 1996: Global observations of oceanic rossby waves. *Science*,  
605    **272** (5259), 234–238.
- 606    Chelton, D. B., M. G. Schlax, and R. M. Samelson, 2011: Global observations of nonlinear  
607    mesoscale eddies. *Progress in Oceanography*, **91** (2), 167–216.
- 608    Chelton, D. B., M. G. Schlax, R. M. Samelson, and R. A. de Szoeke, 2007: Global observations  
609    of large oceanic eddies. *Geophysical Research Letters*, **34** (15), L15 606.

- 610 Cipollini, P., D. Cromwell, P. G. Challenor, and S. Raffaglio, 2001: Rossby waves detected in  
611 global ocean colour data. *Geophysical Research Letters*, **28** (2), 323–326.
- 612 Cipollini, P., D. Cromwell, M. S. Jones, G. D. Quartly, and P. G. Challenor, 1997: Concurrent al-  
613 timeter and infrared observations of rossby wave propagation near 34°N of the northeast atlantic.  
614 *Geophysical Research Letters*, **24** (8), 889–892.
- 615 Dewar, W. K., 1998: On “Too fast” baroclinic planetary waves in the general circulation. *Journal*  
616 *of Physical Oceanography*, **28** (9), 1739–1758.
- 617 Early, J. J., R. M. Samelson, and D. B. Chelton, 2011: The evolution and propagation of quasi-  
618 geostrophic ocean eddies. *Journal of Physical Oceanography*, **41** (8), 1535–1555.
- 619 Ferrari, R., and M. Nikurashin, 2010: Suppression of eddy diffusivity across jets in the southern  
620 ocean. *Journal of Physical Oceanography*, **40** (7), 1501–1519.
- 621 Flierl, G. R., 1978: Models of vertical structure and the calibration of two-layer models. *Dynamics*  
622 *of Atmospheres and Oceans*, **2** (4), 341–381.
- 623 Fu, L., 2009: Pattern and velocity of propagation of the global ocean eddy variability. *Journal of*  
624 *Geophysical Research: Oceans*, **114** (C11), C11 017.
- 625 Gill, A. E., J. S. A. Green, and A. J. Simmons, 1974: Energy partition in the large-scale ocean  
626 circulation and the production of mid-ocean eddies. *Deep Sea Research and Oceanographic*  
627 *Abstracts*, **21** (7), 499–528.
- 628 Gouretski, V., and K. Koltermann, 2004: WOCE global hydrographic climatology. *Berichte des*  
629 *Bundesamtes für Seeschiffahrt und Hydrographie*, 52.

- 630 Hallberg, R., and A. Gnanadesikan, 2006: The role of eddies in determining the structure and re-  
631 sponse of the Wind-Driven southern hemisphere overturning: Results from the modeling eddies  
632 in the southern ocean (MESO) project. *Journal of Physical Oceanography*, **36** (12), 2232–2252.
- 633 Hayashi, Y., 1971: A generalized method of resolving disturbances into progressive and retrogres-  
634 sive waves by space fourier and time Cross-Spectral analyses. *Journal of the Meteorological  
635 Society of Japan. Ser. II*, **49** (2), 125–128.
- 636 Held, I. M., and V. D. Larichev, 1996: A scaling theory for horizontally homogeneous, baroclini-  
637 cally unstable flow on a beta plane. *Journal of the Atmospheric Sciences*, **53** (7), 946–952.
- 638 Hill, K. L., I. S. Robinson, and P. Cipollini, 2000: Propagation characteristics of extratropical  
639 planetary waves observed in the ATSR global sea surface temperature record. *Journal of Geo-  
640 physical Research: Oceans*, **105** (C9), 21 927–21 945.
- 641 Jansen, M. F., A. J. Adcroft, R. Hallberg, and I. M. Held, 2015: Parameterization of eddy fluxes  
642 based on a mesoscale energy budget. *Ocean Modelling*, **92**, 28–41.
- 643 Jansen, M. F., and I. M. Held, 2014: Parameterizing subgrid-scale eddy effects using energetically  
644 consistent backscatter. *Ocean Modelling*, **80**, 36–48.
- 645 Johnson, G. C., and H. L. Bryden, 1989: On the size of the antarctic circumpolar current. *Deep  
646 Sea Research Part A. Oceanographic Research Papers*, **36** (1), 39–53.
- 647 Killworth, P. D., and J. R. Blundell, 2003: Long extratropical planetary wave propagation in the  
648 presence of slowly varying mean flow and bottom topography. part i: The local problem. *Journal  
649 of Physical Oceanography*, **33** (4), 784–801.

- 650 Killworth, P. D., and J. R. Blundell, 2004: The dispersion relation for planetary waves in the pres-  
651 ence of mean flow and topography. part i: Analytical theory and One-Dimensional examples.  
652 *Journal of Physical Oceanography*, **34** (12), 2692–2711.
- 653 Killworth, P. D., and J. R. Blundell, 2005: The dispersion relation for planetary waves in the  
654 presence of mean flow and topography. part II: Two-Dimensional examples and global results.  
655 *Journal of Physical Oceanography*, **35** (11), 2110–2133.
- 656 Killworth, P. D., and J. R. Blundell, 2007: Planetary wave response to surface forcing and insta-  
657 bility in the presence of mean flow and topography. *Journal of Physical Oceanography*, **37** (5),  
658 1297–1320.
- 659 Killworth, P. D., D. B. Chelton, and R. A. de Szoeke, 1997: The speed of observed and theoretical  
660 long extratropical planetary waves. *Journal of Physical Oceanography*, **27** (9), 1946–1966.
- 661 Klocker, A., and R. Abernathey, 2013: Global patterns of mesoscale eddy properties and diffusiv-  
662 ities. *Journal of Physical Oceanography*, **44** (3), 1030–1046.
- 663 Klocker, A., R. Ferrari, and J. H. LaCasce, 2012a: Estimating suppression of eddy mixing by  
664 mean flows. *Journal of Physical Oceanography*, **42** (9), 1566–1576.
- 665 Klocker, A., R. Ferrari, J. H. Lacasce, and S. T. Merrifield, 2012b: Reconciling float-based and  
666 tracer-based estimates of lateral diffusivities. *Journal of Marine Research*, **70** (4), 569–602.
- 667 Klocker, A., and D. P. Marshall, 2014: Advection of baroclinic eddies by depth mean flow. *Geo-  
668 physical Research Letters*, **41** (10), 3517–3521.
- 669 Maltrud, M., and G. Vallis, 1991: Energy spectra and coherent structures in forced two-  
670 dimensional and beta-plane turbulence. *Journal of Fluid Mechanics*, **228**, 321–342.

- 671 Marshall, J., E. Shuckburgh, H. Jones, and C. Hill, 2006: Estimates and implications of sur-  
672 face eddy diffusivity in the southern ocean derived from tracer transport. *Journal of Physical*  
673 *Oceanography*, **36** (9), 1806–1821.
- 674 Mazloff, M. R., P. Heimbach, and C. Wunsch, 2010: An Eddy-Permitting southern ocean state  
675 estimate. *Journal of Physical Oceanography*, **40** (5), 880–899.
- 676 Mcwilliams, J. C., 2008: The nature and consequences of oceanic eddies. *Ocean Modeling in an*  
677 *Eddying Regime*, t. W. Hecht, and H. Hasumi, Eds., American Geophysical Union, 5–15.
- 678 McWilliams, J. C., and G. R. Flierl, 1979: On the evolution of isolated, nonlinear vortices. *Journal*  
679 *of Physical Oceanography*, **9** (6), 1155–1182.
- 680 Nof, D., 1981: On the  $\beta$ -Induced movement of isolated baroclinic eddies. *Journal of Physical*  
681 *Oceanography*, **11** (12), 1662–1672.
- 682 Pedlosky, J., 1979: *Geophysical Fluid Dynamics*. Springer Verlag.
- 683 Qiu, B., S. Chen, P. Klein, H. Sasaki, and Y. Sasai, 2014: Seasonal mesoscale and submesoscale  
684 eddy variability along the North Pacific subtropical countercurrent. *J. Phys. Oceanogr.*, **44**,  
685 3079–3098.
- 686 Randel, W. J., and I. M. Held, 1991: Phase speed spectra of transient eddy fluxes and critical layer  
687 absorption. *Journal of the Atmospheric Sciences*, **48** (5), 688–697.
- 688 Rhines, P. B., 1975: Waves and turbulence on a beta-plane. *Journal of Fluid Mechanics*, **69** (03),  
689 417–443.
- 690 Rhines, P. B., 1979: Geostrophic turbulence. *Annual Review of Fluid Mechanics*, **11** (1), 401–441.

- 691 Salmon, R., 1980: Baroclinic instability and geostrophic turbulence. *Geophysical & Astrophysical*  
692 *Fluid Dynamics*, **15** (1), 167–211.
- 693 Stammer, D., 1997: Global characteristics of ocean variability estimated from regional  
694 TOPEX/POSEIDON altimeter measurements. *Journal of Physical Oceanography*, **27** (8),  
695 1743–1769.
- 696 Taylor, G. I., 1938: The spectrum of turbulence. *Proceedings of the Royal Society of London.*  
697 *Series A - Mathematical and Physical Sciences*, **164** (919), 476–490.
- 698 Thompson, A., and W. Young, 2007: Two-layer baroclinic eddy heat fluxes: Zonal flows and  
699 energy balance. *J. Atmos. Sci.*, **64**, 3214–3231.
- 700 Tulloch, R., J. Marshall, C. Hill, and K. S. Smith, 2011: Scales, growth rates, and spectral fluxes  
701 of baroclinic instability in the ocean. *Journal of Physical Oceanography*, **41** (6), 1057–1076.
- 702 Tulloch, R., J. Marshall, and K. S. Smith, 2009: Interpretation of the propagation of surface  
703 altimetric observations in terms of planetary waves and geostrophic turbulence. *Journal of Geo-*  
704 *physical Research: Oceans*, **114** (C2), C02 005.
- 705 Vallis, G. K., 2006: *Atmospheric and Oceanic Fluid Dynamics*. Cambridge University Press.
- 706 Waterman, S., N. G. Hogg, and S. R. Jayne, 2011: Eddy–Mean flow interaction in the kuroshio  
707 extension region. *Journal of Physical Oceanography*, **41** (6), 1182–1208.
- 708 Wortham, C., J. Callies, and M. G. Scharffenberg, 2014: Asymmetries between wavenumber  
709 spectra of along- and Across-Track velocity from tandem mission altimetry. *Journal of Physical*  
710 *Oceanography*, **44** (4), 1151–1160.

- 711 Wortham, C. J. L., 2013: *A multi-dimensional spectral description of ocean variability with ap-*  
712 *plications*. Massachusetts Institute of Technology and Woods Hole Oceanographic Institution,  
713 Woods Hole, MA.
- 714 Wunsch, C., 1997: The vertical partition of oceanic horizontal kinetic energy. *Journal of Physical*  
715 *Oceanography*, **27** (8), 1770–1794.
- 716 Wunsch, C., 2009: The oceanic variability spectrum and transport trends. *Atmosphere-Ocean*,  
717 **47** (4), 281–291.
- 718 Wunsch, C., and P. Heimbach, 2007: Practical global oceanic state estimation. *Physica D: Non-*  
719 *linear Phenomena*, **230** (1–2), 197–208.
- 720 Zang, X., and C. Wunsch, 1999: The observed dispersion relationship for north pacific rossby  
721 wave motions. *Journal of Physical Oceanography*, **29** (9), 2183–2190.
- 722 Zhai, X., H. L. Johnson, and D. P. Marshall, 2010: Significant sink of ocean-eddy energy near  
723 western boundaries. *Nature Geoscience*, **3** (9), 608–612.

724 LIST OF FIGURES

- Fig. 1.** Linear baroclinic instability calculation for a two-layer QG model with the parameters  $\delta = 0.25$  and  $\Delta U = 0.04$  m/s. The upper panel shows the growth rate per day of the unstable mode as a function of zonal inverse wavelength normalized by that of the baroclinic radius of deformation  $L_d = 15$  km. The lower panel shows the phase speed of these unstable modes. Black, blue, magenta and red curves correspond to no bottom friction case,  $(10 \text{ days})^{-1}$  decay rate,  $(20 \text{ days})^{-1}$  decay rate and  $(40 \text{ days})^{-1}$  decay rate, respectively. Dashed, dash-dot, and dotted curves correspond to the phase speeds for reduced-gravity mode, barotropic mode, and baroclinic mode, respectively. . . . .

**Fig. 2.** Hovmöller diagram of upper layer streamfunction for two-layer QG model as a function of longitude and time. The strong friction experiment (left panel) has bottom friction with  $(10 \text{ days})^{-1}$  decay rate, control experiment (middle panel) with  $(20 \text{ days})^{-1}$  decay rate, and the weak friction experiment (right panel) with  $(40 \text{ days})^{-1}$  decay rate. For each panel, the upper layer streamfunction is normalized with respect to the maximum absolute value within the period to highlight the propagation pattern. . . . .

**Fig. 3.** Power spectrum of EKE ( $|(k^2 + l^2)\widehat{\psi_1}^2|/2$ ) as a function of zonal wavenumber  $k$  and meridional wavenumber  $l$  for the same three two-layer QG experiments as in Fig. 2. . . . .

**Fig. 4.** The same three experiments as shown in Fig. 2. The three curves show the ratios between barotropic EKE and the total EKE of the two layers. The abscissa is zonal wavenumber normalized by the zonal wavenumber corresponding to the deformation radius. . . . .

**Fig. 5.** The ratios between barotropic EKE and total EKE from the two-layer QG experiments, varying respective non-dimensional parameters. The varied non-dimensional parameters are layer thickness ratio (left), frictional strength (middle), and non-dimensional beta (right). . . . .

**Fig. 6.** The top row shows spectral energy budget analysis for the nonlinear two-layer QG simulations as a function of zonal inverse wavelength normalized by radius of deformation as abscissa and the respective non-dimensional parameters as ordinate, i.e. the layer thickness ratio (left column), friction strength (second column), and criticality (third and fourth columns). The conversion from available potential energy to eddy kinetic energy is shown in blue shading and the barotropic EKE in yellow-to-red contour lines. Both spectral budgets are normalized with respect to their maximum value at each non-dimensional parameter. The contour intervals are identical between the four panels. The bottom shows the linear baroclinic growth rate as a function of zonal inverse wavelength normalized by radius of deformation as abscissa and respective non-dimensional parameters as ordinate. The first contour corresponds to a growth rate of 0.001 per day, and contour intervals are 0.003 per day. . . . .

**Fig. 7.** Power spectra (top row) of cross-track EKE as a function of frequency and zonal inverse wavelength for the same three two-layer QG experiments as in Fig. 2. The middle row is the same as the top row, except normalized at each zonal inverse wavelength band. The bottom row shows the cross-track EKE power spectra as a function of zonal phase speed and zonal inverse wavelength. In all panels, dispersion relation curves for the baroclinic mode  $C_{BC}$  in the long wave limit (cyan), reduced-gravity mode  $C_{RG}$  (blue) and barotropic mode  $C_{BT}$  (green) are plotted on top of power spectra. For the reduced-gravity mode and barotropic mode, the solid curves assume  $l = 0$ , while the dashed curves assume  $l = k$ . The linear unstable mode is presented in white dots with varying marker sizes corresponding to its growth rate. The zero phase speed line is highlighted in white. . . . .

769	<b>Fig. 8.</b> Cross-track EKE power spectra (top row) in the nonlinear two-layer QG simulations as a function of zonal phase speed and respective non-dimensional parameters (same order as used in Fig. 6). Dispersion relation curves of the baroclinic mode in long wave limit (cyan), reduced-gravity mode (blue) and barotropic mode (green) are plotted on top of the power spectra. For the reduced-gravity and barotropic modes, the solid curves assume $l = 0$ , while the dashed curves assume $l = k$ . See text for more details. Bottom row shows the linear growth rate; similar as in Fig. 6, but as a function of phase speed in the abscissa. In all panels, the zero phase speed line is highlighted in white. . . . .	45
770		
771		
772		
773		
774		
775		
776		
777	<b>Fig. 9.</b> Zonal component of the absolute geostrophic velocity of the AVISO product averaged from year 2012. Two sections chosen for analysis are marked by green lines. . . . .	46
778		
779		
780		
781		
782		
783		
784		
785	<b>Fig. 10.</b> The top row shows zonally-averaged neutral densities (upper left panel) and the corresponding first baroclinic mode structure (upper right panel) for the two considered sections (see legend). The bottom row shows the projection of the full continuous zonally-averaged zonal flow velocity profile for the two sections onto the barotropic and first baroclinic modes (see text for an explanation of the analog two-layer model.) Note the different ranges in the abscissa between the bottom left and right panels. . . . .	47
786		
787	<b>Fig. 11.</b> Hovmöller diagram of meridional geostrophic velocity anomalies from AVISO as a function of longitude and time, at 27.625 N (left) and 57.625 S (right). . . . .	48
788		
789		
790		
787	<b>Fig. 12.</b> Similar to Figure 8, but for the AVISO data during 1993-2004 at the two sections, 27.625 N (left column) and 57.625 S (right column). In addition to the dispersion relations shown in Figure 8, the dash-dotted blue line here shows the long-wave limit of the reduced gravity mode. . . . .	49
788		

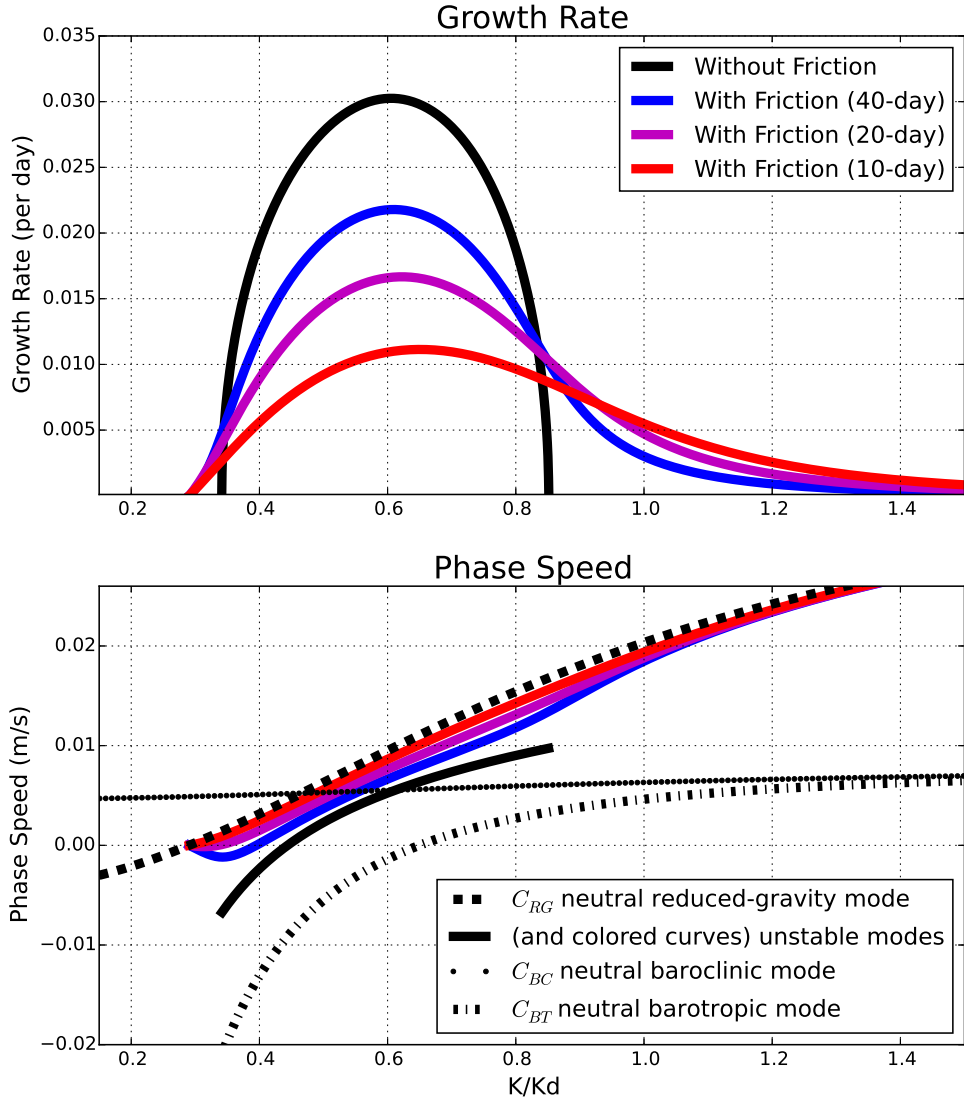
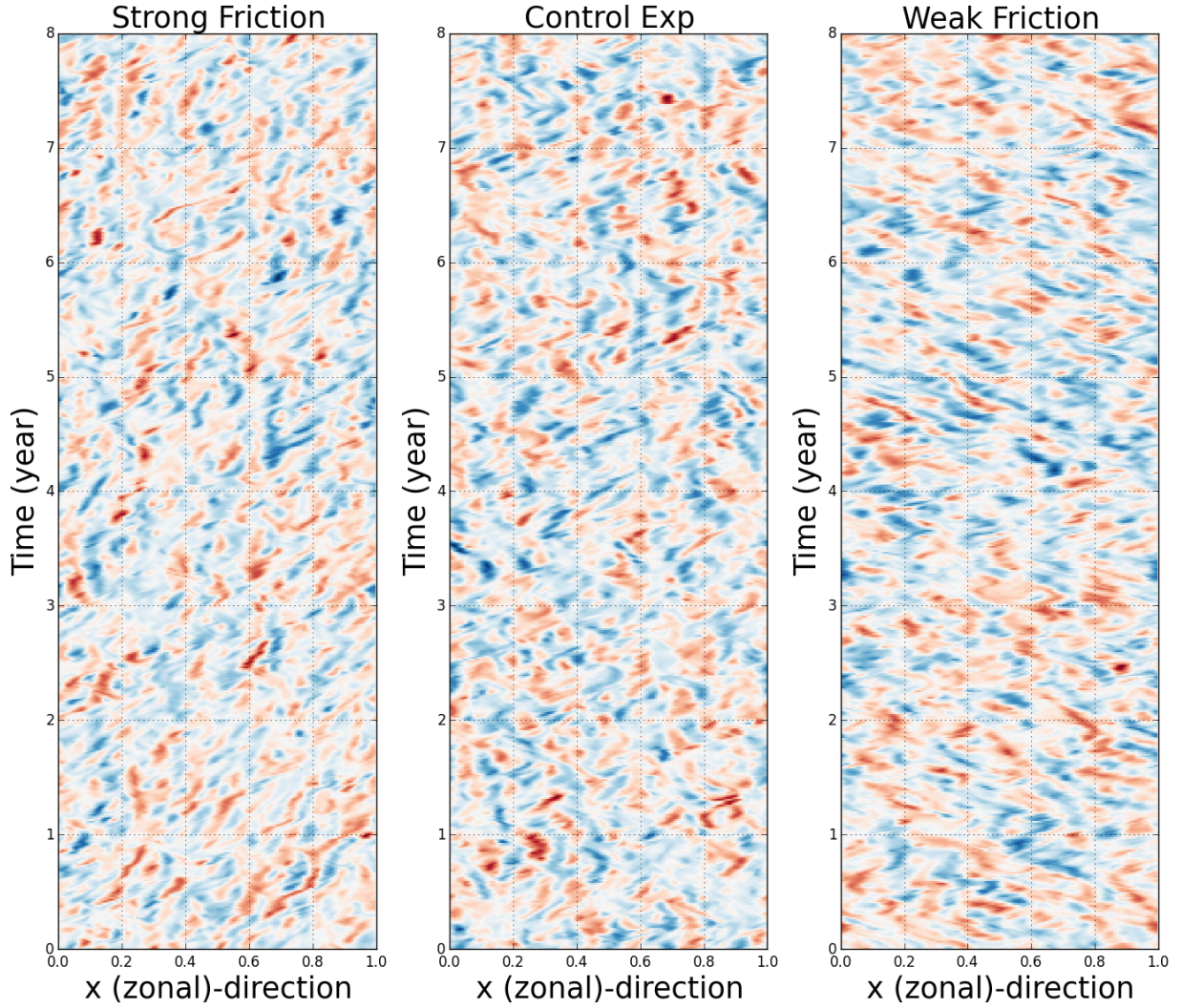


FIG. 1. Linear baroclinic instability calculation for a two-layer QG model with the parameters  $\delta = 0.25$  and  $\Delta U = 0.04$  m/s. The upper panel shows the growth rate per day of the unstable mode as a function of zonal inverse wavelength normalized by that of the baroclinic radius of deformation  $L_d = 15$  km. The lower panel shows the phase speed of these unstable modes. Black, blue, magenta and red curves correspond to no bottom friction case,  $(10 \text{ days})^{-1}$  decay rate,  $(20 \text{ days})^{-1}$  decay rate and  $(40 \text{ days})^{-1}$  decay rate, respectively. Dashed, dash-dot, and dotted curves correspond to the phase speeds for reduced-gravity mode, barotropic mode, and baroclinic mode, respectively.



798 FIG. 2. Hovmöller diagram of upper layer streamfunction for two-layer QG model as a function of longitude  
 799 and time. The strong friction experiment (left panel) has bottom friction with  $(10 \text{ days})^{-1}$  decay rate, control  
 800 experiment (middle panel) with  $(20 \text{ days})^{-1}$  decay rate, and the weak friction experiment (right panel) with  $(40$   
 801  $\text{days})^{-1}$  decay rate. For each panel, the upper layer streamfunction is normalized with respect to the maximum  
 802 absolute value within the period to highlight the propagation pattern.

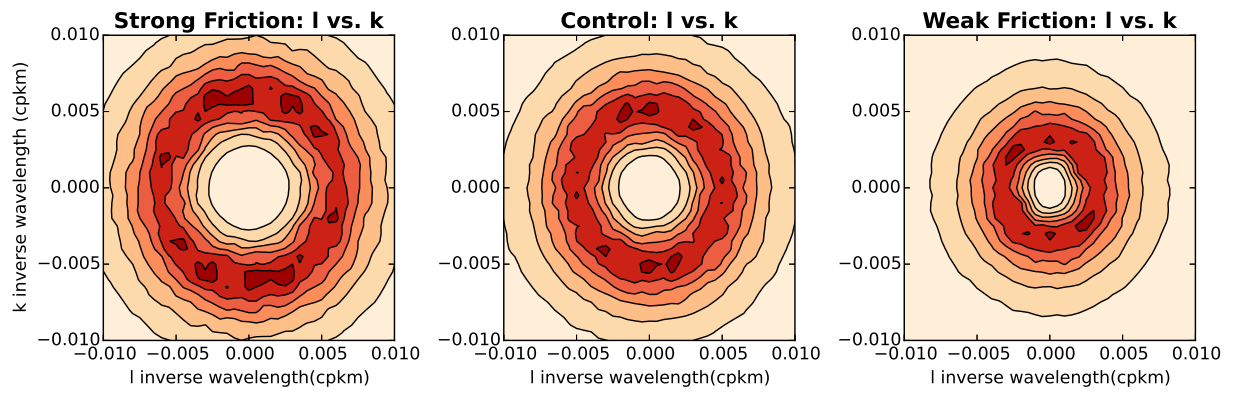
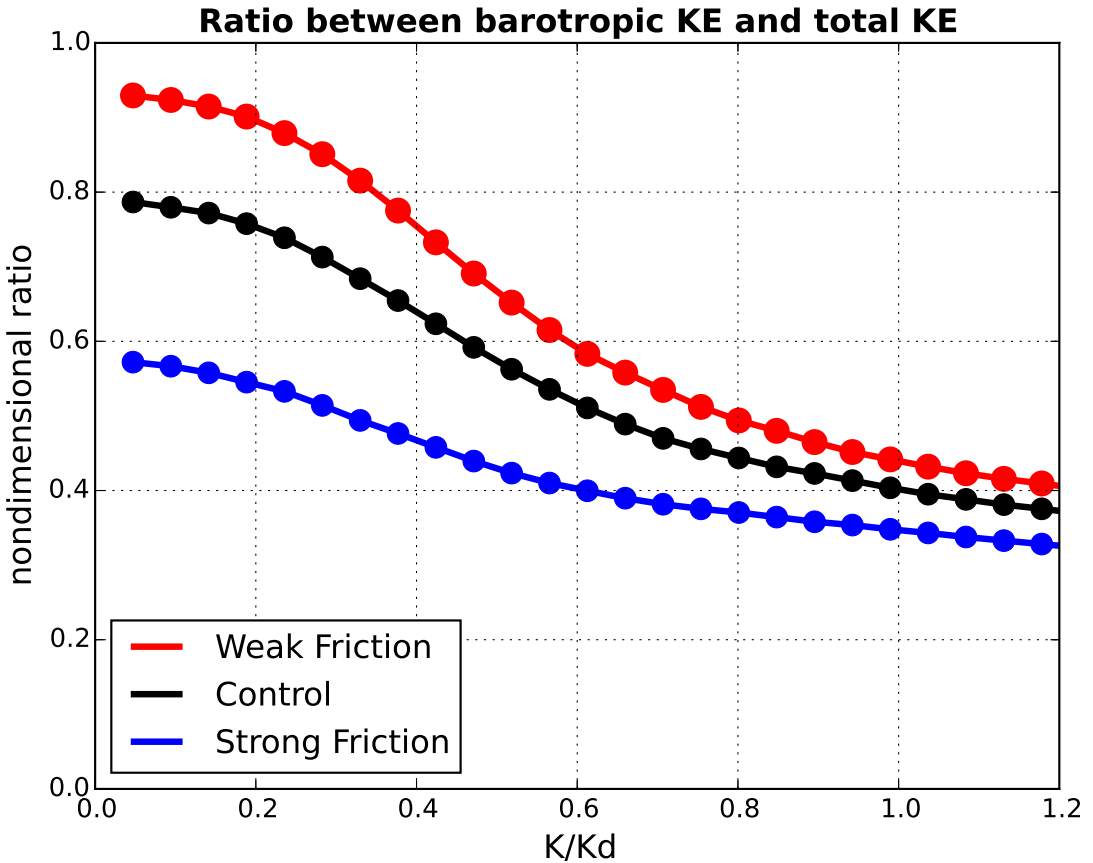
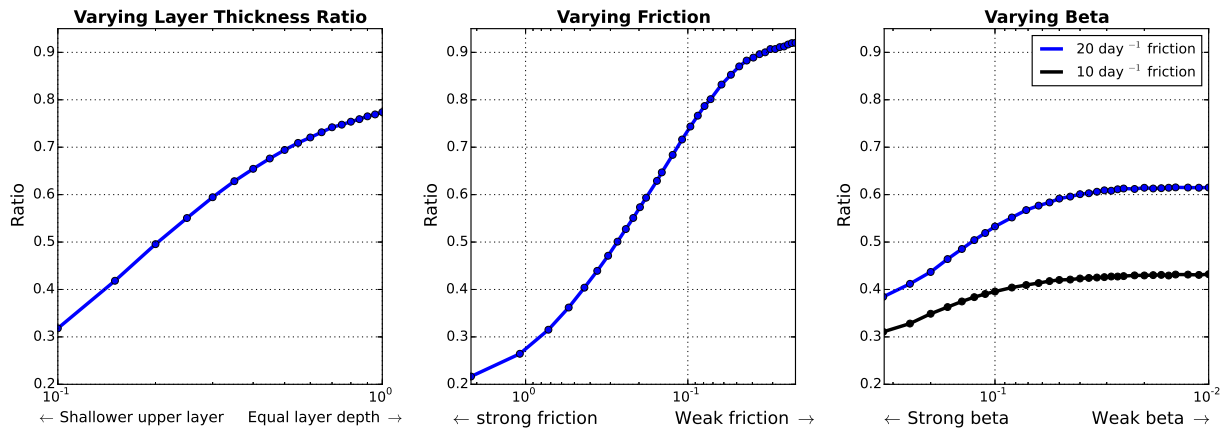


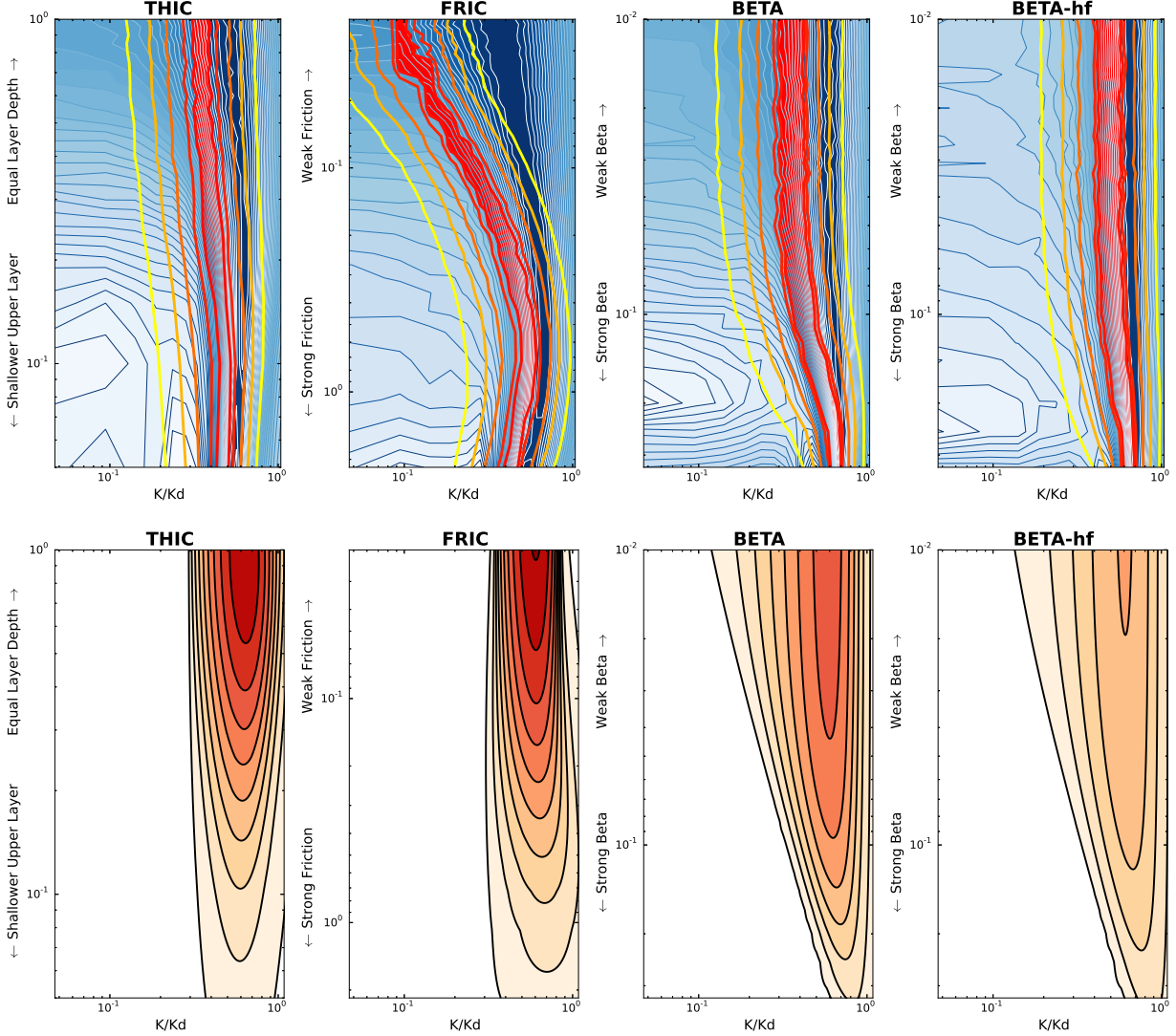
FIG. 3. Power spectrum of EKE ( $|(|k^2 + l^2| \widehat{\psi}_1^2)|/2$ ) as a function of zonal wavenumber  $k$  and meridional wavenumber  $l$  for the same three two-layer QG experiments as in Fig. 2.



805 FIG. 4. The same three experiments as shown in Fig. 2. The three curves show the ratios between barotropic  
 806 EKE and the total EKE of the two layers. The abscissa is zonal wavenumber normalized by the zonal wavenum-  
 807 ber corresponding to the deformation radius.



808 FIG. 5. The ratios between barotropic EKE and total EKE from the two-layer QG experiments, varying  
 809 respective non-dimensional parameters. The varied non-dimensional parameters are layer thickness ratio (left),  
 810 frictional strength (middle), and non-dimensional beta (right).



811 FIG. 6. The top row shows spectral energy budget analysis for the nonlinear two-layer QG simulations as  
 812 a function of zonal inverse wavelength normalized by radius of deformation as abscissa and the respective  
 813 non-dimensional parameters as ordinate, i.e. the layer thickness ratio (left column), friction strength (second  
 814 column), and criticality (third and fourth columns). The conversion from available potential energy to eddy  
 815 kinetic energy is shown in blue shading and the barotropic EKE in yellow-to-red contour lines. Both spectral  
 816 budgets are normalized with respect to their maximum value at each non-dimensional parameter. The contour  
 817 intervals are identical between the four panels. The bottom shows the linear baroclinic growth rate as a function  
 818 of zonal inverse wavelength normalized by radius of deformation as abscissa and respective non-dimensional  
 819 parameters as ordinate. The first contour corresponds to a growth rate of 0.001 per day, and contour intervals are  
 820 0.003 per day.

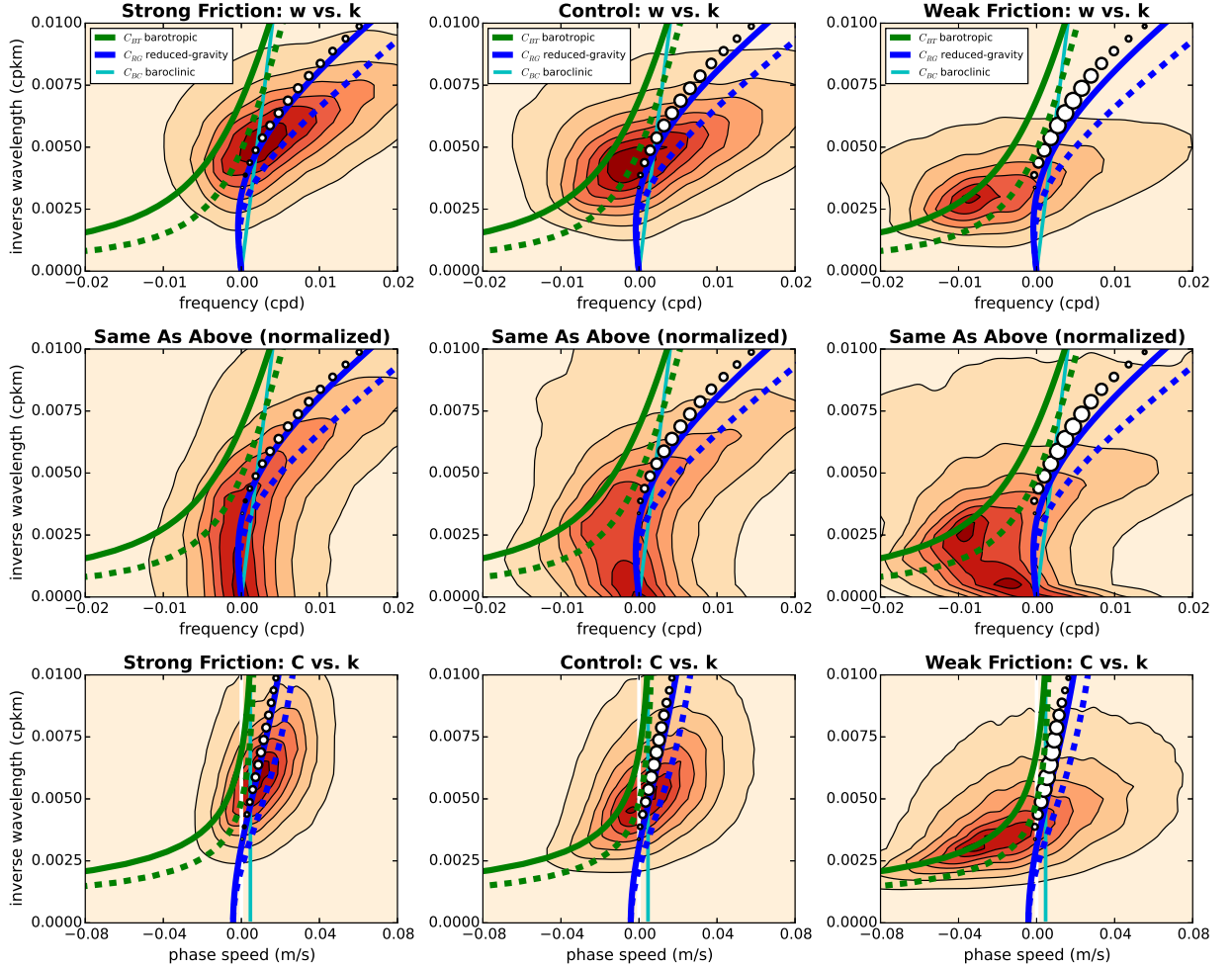
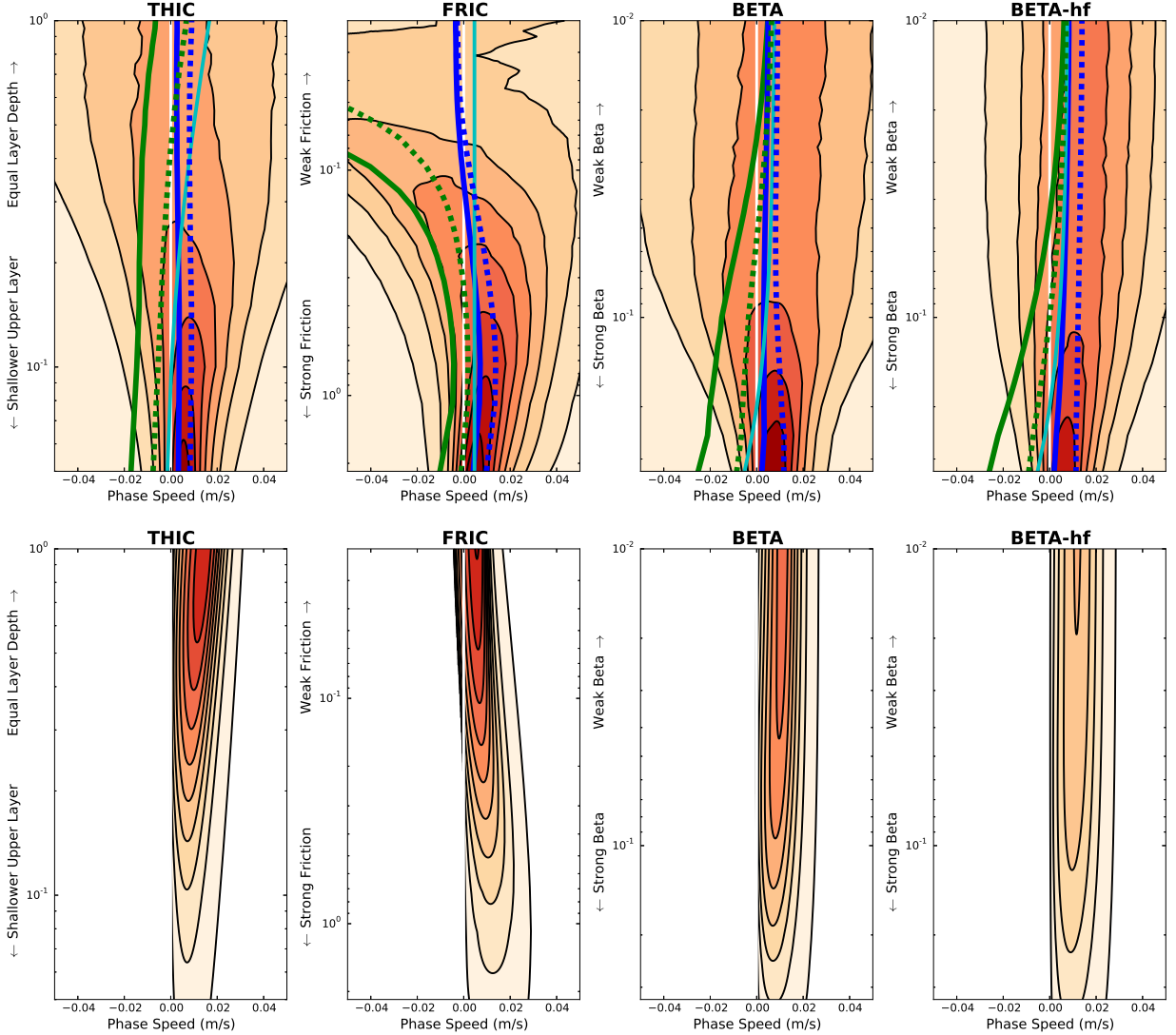
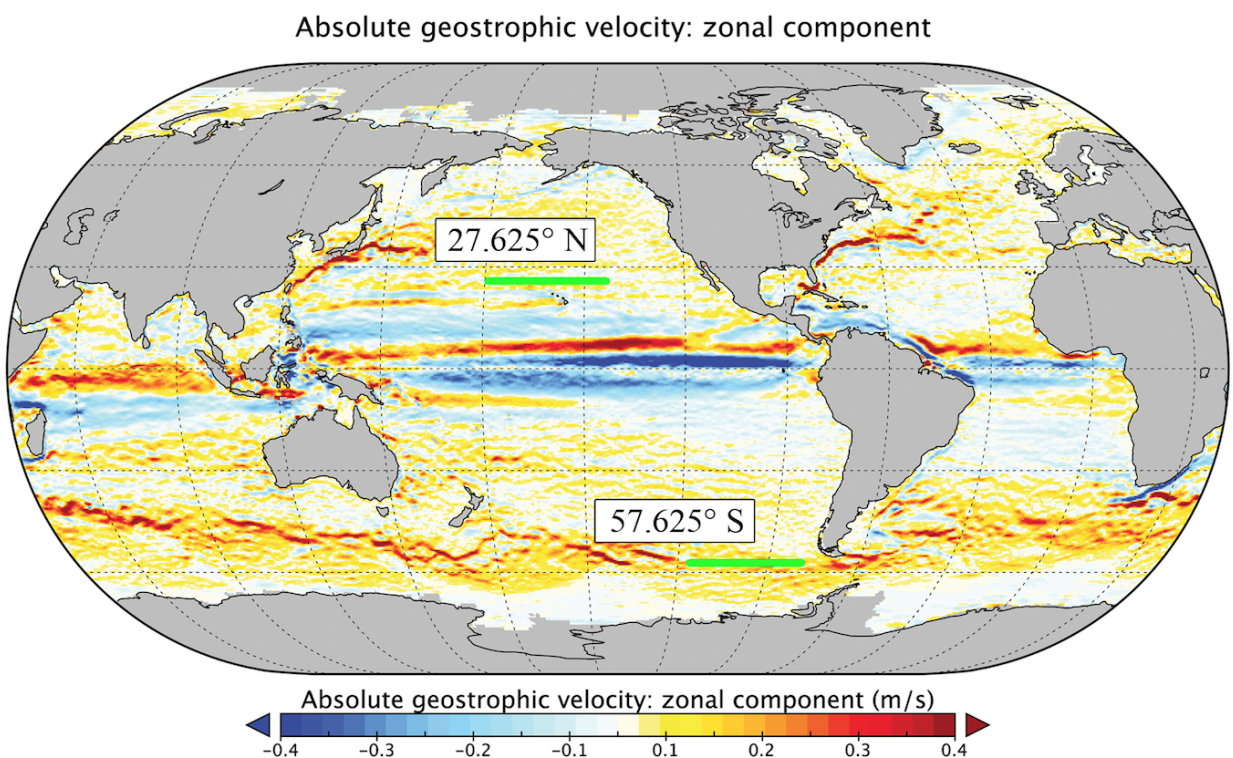


FIG. 7. Power spectra (top row) of cross-track EKE as a function of frequency and zonal inverse wavelength for the same three two-layer QG experiments as in Fig. 2. The middle row is the same as the top row, except normalized at each zonal inverse wavelength band. The bottom row shows the cross-track EKE power spectra as a function of zonal phase speed and zonal inverse wavelength. In all panels, dispersion relation curves for the baroclinic mode  $C_{BC}$  in the long wave limit (cyan), reduced-gravity mode  $C_{RG}$  (blue) and barotropic mode  $C_{BT}$  (green) are plotted on top of power spectra. For the reduced-gravity mode and barotropic mode, the solid curves assume  $l = 0$ , while the dashed curves assume  $l = k$ . The linear unstable mode is presented in white dots with varying marker sizes corresponding to its growth rate. The zero phase speed line is highlighted in white.



829 FIG. 8. Cross-track EKE power spectra (top row) in the nonlinear two-layer QG simulations as a function  
 830 of zonal phase speed and respective non-dimensional parameters (same order as used in Fig. 6). Dispersion  
 831 relation curves of the baroclinic mode in long wave limit (cyan), reduced-gravity mode (blue) and barotropic  
 832 mode (green) are plotted on top of the power spectra. For the reduced-gravity and barotropic modes, the solid  
 833 curves assume  $l = 0$ , while the dashed curves assume  $l = k$ . See text for more details. Bottom row shows the  
 834 linear growth rate; similar as in Fig. 6, but as a function of phase speed in the abscissa. In all panels, the zero  
 835 phase speed line is highlighted in white.



836 FIG. 9. Zonal component of the absolute geostrophic velocity of the AVISO product averaged from year 2012.  
837 Two sections chosen for analysis are marked by green lines.

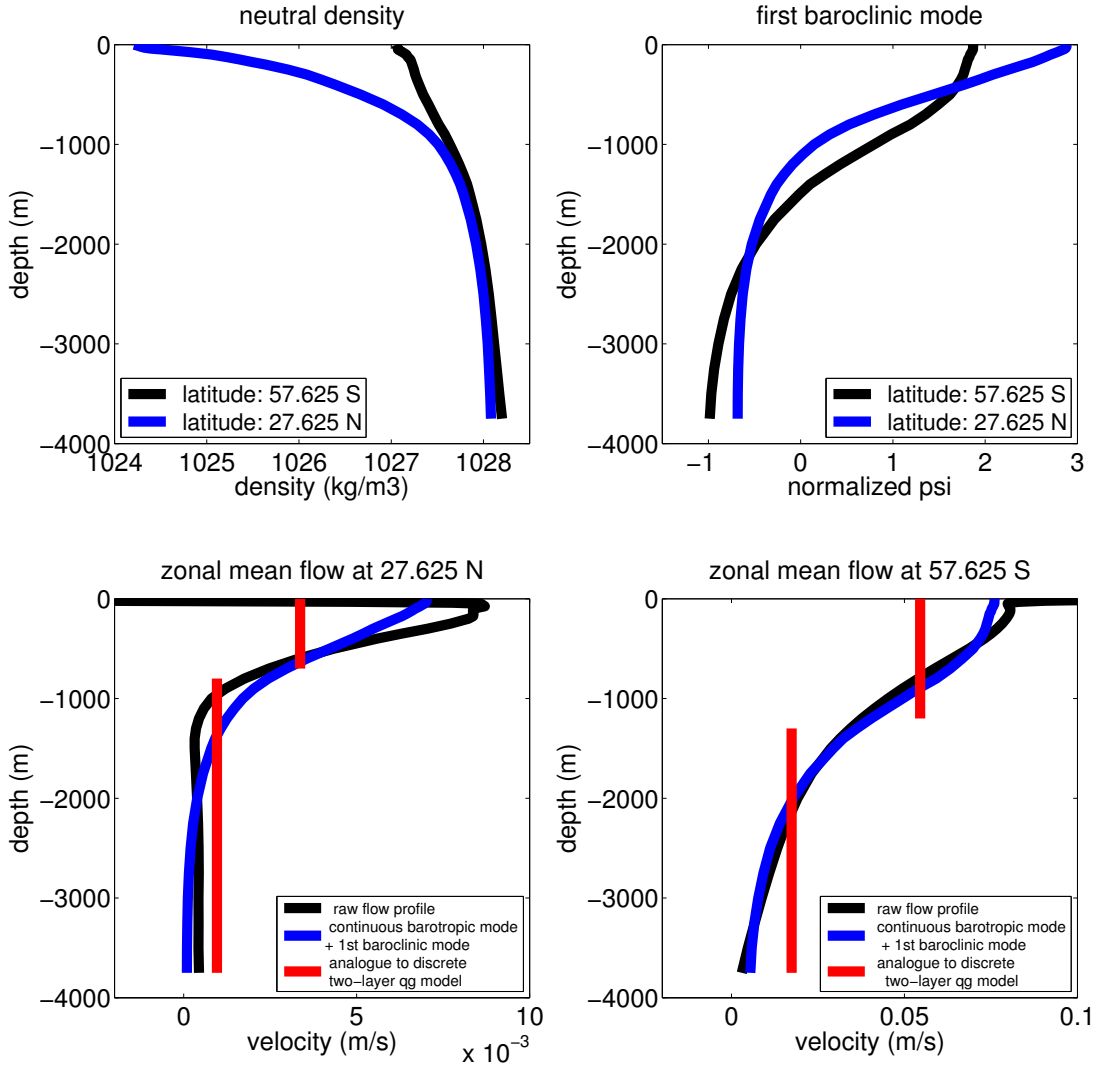


FIG. 10. The top row shows zonally-averaged neutral densities (upper left panel) and the corresponding first baroclinic mode structure (upper right panel) for the two considered sections (see legend). The bottom row shows the projection of the full continuous zonally-averaged zonal flow velocity profile for the two sections onto the barotropic and first baroclinic modes (see text for an explanation of the analog two-layer model.) Note the different ranges in the abscissa between the bottom left and right panels.

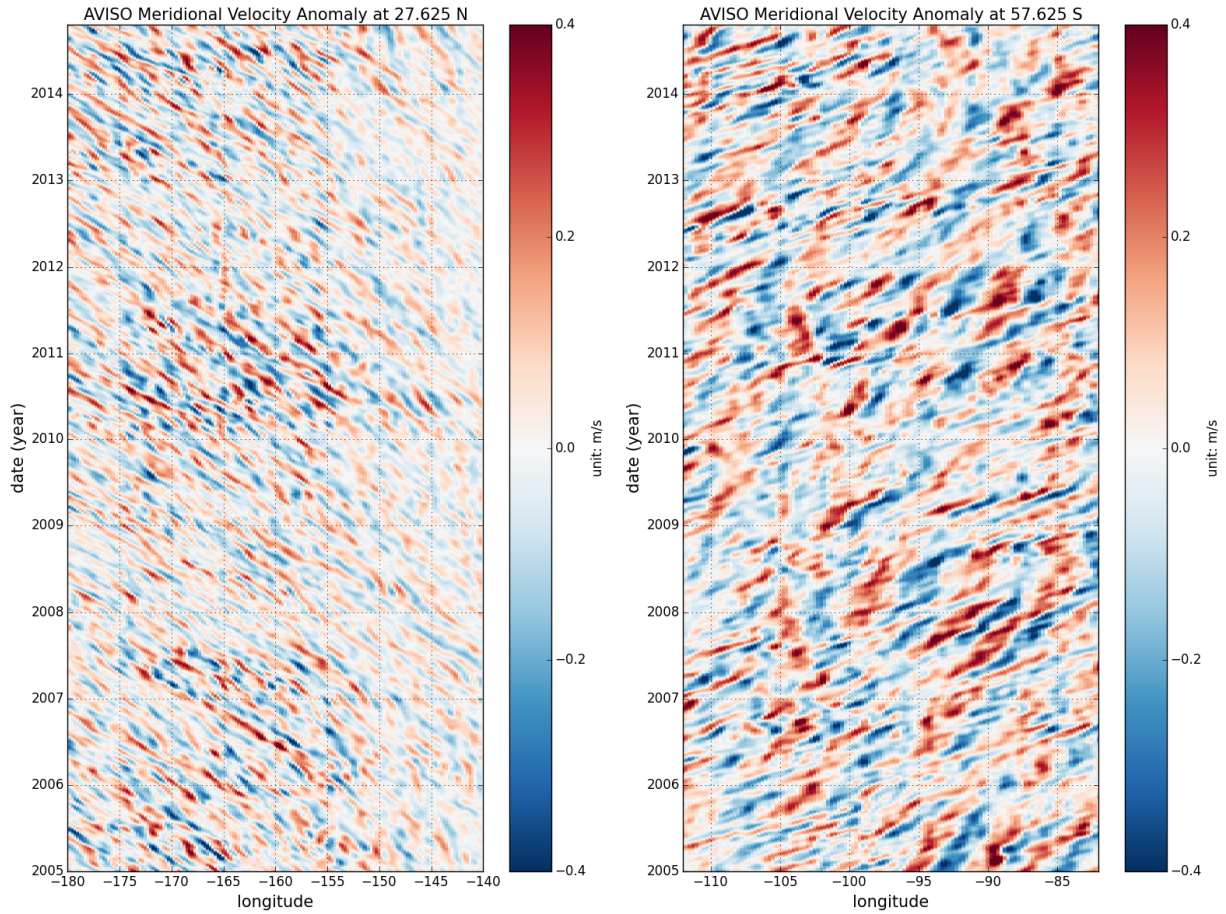


FIG. 11. Hovmöller diagram of meridional geostrophic velocity anomalies from AVISO as a function of longitude and time, at 27.625 N (left) and 57.625 S (right).

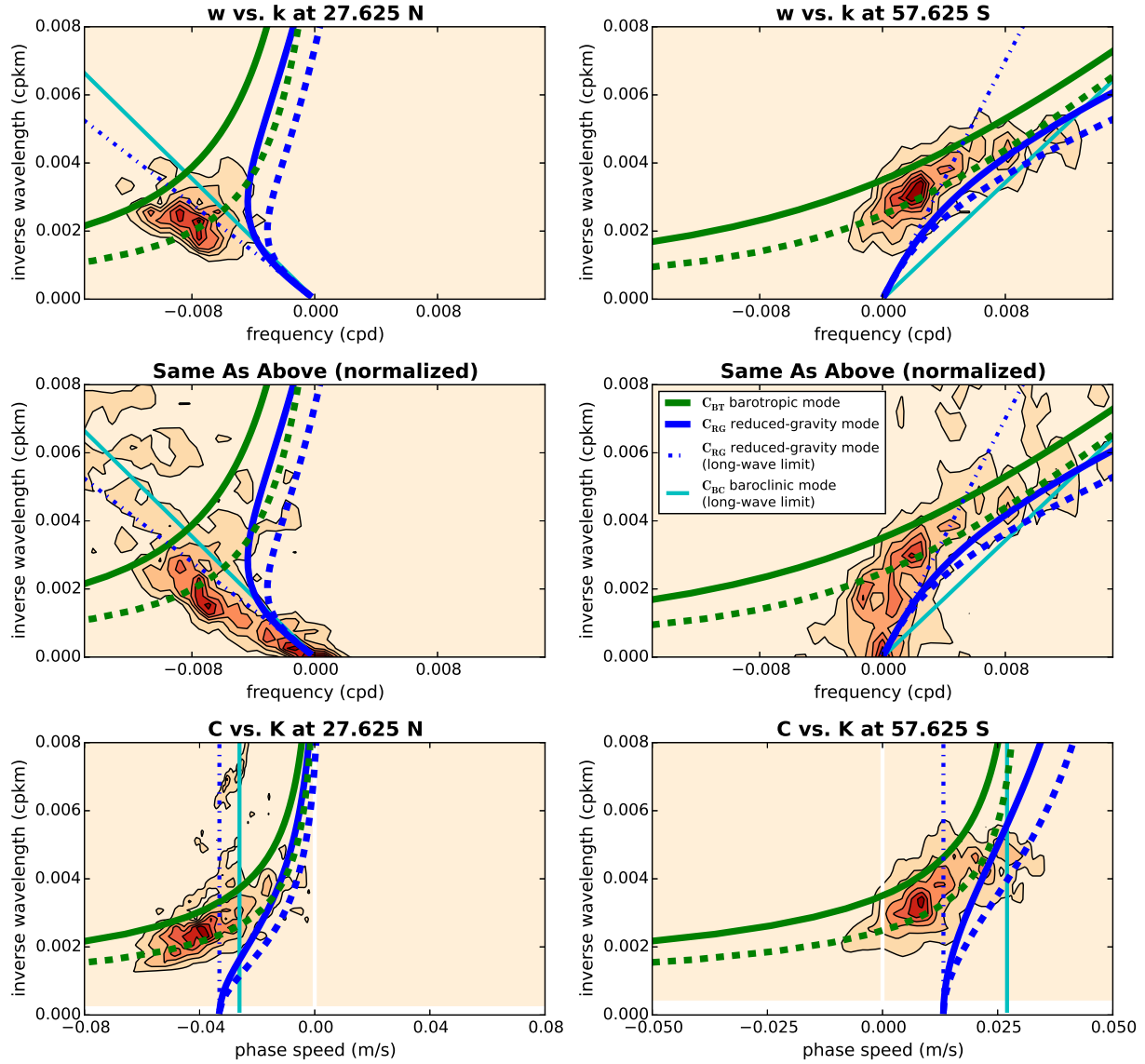


FIG. 12. Similar to Figure 8, but for the AVISO data during 1993-2004 at the two sections, 27.625 N (left column) and 57.625 S (right column). In addition to the dispersion relations shown in Figure 8, the dash-dotted blue line here shows the long-wave limit of the reduced gravity mode.